



HAL
open science

Partitioning of Mg, Sr, Ba and U into a subaqueous speleothem.

Russell N. Drysdale, Giovanni Zanchetta, Ilaria Baneschi, Massimo Guidi, Ilaria Isola, Isabelle Couchoud, Leonardo Piccinini, Alan Greig, Henry Wong, Jon Woodhead, et al.

► **To cite this version:**

Russell N. Drysdale, Giovanni Zanchetta, Ilaria Baneschi, Massimo Guidi, Ilaria Isola, et al.. Partitioning of Mg, Sr, Ba and U into a subaqueous speleothem.. *Geochimica et Cosmochimica Acta*, 2019, 264, pp.67-91. 10.1016/j.gca.2019.08.001 . hal-02415970

HAL Id: hal-02415970

<https://hal.science/hal-02415970v1>

Submitted on 20 Dec 2021

HAL is a multi-disciplinary open access archive for the deposit and dissemination of scientific research documents, whether they are published or not. The documents may come from teaching and research institutions in France or abroad, or from public or private research centers.

L'archive ouverte pluridisciplinaire **HAL**, est destinée au dépôt et à la diffusion de documents scientifiques de niveau recherche, publiés ou non, émanant des établissements d'enseignement et de recherche français ou étrangers, des laboratoires publics ou privés.



Distributed under a Creative Commons Attribution - NonCommercial 4.0 International License

21 **ABSTRACT**

22 The trace-element geochemistry of speleothems is becoming increasingly used for reconstructing
23 palaeoclimate, with a particular emphasis on elements whose concentrations vary according to
24 hydrological conditions at the cave site (e.g. Mg, Sr, Ba and U). An important step in interpreting
25 trace-element abundances is understanding the underlying processes of their incorporation. This
26 includes quantifying the fractionation between the solution and speleothem carbonate via partition
27 coefficients (where the partitioning (D) of element X (D_X) is the molar ratio $[X/Ca]$ in the calcite
28 divided by the molar ratio $[X/Ca]$ in the parent water) and evaluating the degree of spatial
29 variability across time-constant speleothem layers. Previous studies of how these elements are
30 incorporated into speleothems have focused primarily on stalagmites and their source waters in
31 natural cave settings, or have used synthetic solutions under cave-analogue laboratory conditions to
32 produce similar dripstones. However, dripstones are not the only speleothem types capable of
33 yielding useful palaeoclimate information. In this study, we investigate the incorporation of Mg, Sr,
34 Ba and U into a subaqueous calcite speleothem (CD3) growing in a natural cave pool in Italy. Pool-
35 water measurements extending back 15 years reveal a remarkably stable geochemical environment
36 owing to the deep cave setting, enabling the calculation of precise solution $[X/Ca]$. We determine
37 the trace element variability of ‘modern’ subaqueous calcite from a drill core taken through CD3 to
38 derive D_{Mg} , D_{Sr} , D_{Ba} and D_U then compare these with published cave, cave-analogue and seawater-
39 analogue studies. The D_{Mg} for CD3 is anomalously high (0.042 ± 0.002) compared to previous
40 estimates at similar temperatures ($\sim 8^\circ\text{C}$). The D_{Sr} (0.100 ± 0.007) is similar to previously reported
41 values, but data from this study as well as those from Tremaine and Froelich (2013) and Day and
42 Henderson (2013) suggest that $[Na/Sr]$ might play an important role in Sr incorporation through the
43 potential for Na to outcompete Sr for calcite non-lattice sites. D_{Ba} in CD3 (0.086 ± 0.008) is similar
44 to values derived by Day and Henderson (2013) under cave-analogue conditions, whilst D_U (0.013
45 ± 0.002) is almost an order of magnitude lower, possibly due to the unusually slow speleothem
46 growth rates ($<1 \mu\text{m a}^{-1}$), which could expose the crystal surfaces to leaching of uranyl carbonate.
47 Finally, laser-ablation ICP-MS analysis of the upper $7 \mu\text{m}$ of CD3, regarded as ‘modern’ for the
48 purposes of this study, reveals considerable heterogeneity, particularly for Sr, Ba and U, which is
49 potentially indicative of compositional zoning. This reinforces the need to conduct 2D mapping
50 and/or multiple laser passes to capture the range of time-equivalent elemental variations prior to
51 palaeoclimate interpretation.

52

53 **Keywords:** trace-element geochemistry, speleothems, calcite, partition coefficients, caves,
54 palaeoclimate

55

56 **1. INTRODUCTION AND BACKGROUND**

57 The trace-element geochemistry of calcium carbonate minerals is widely used to help reconstruct
58 past environments across a wide range of time scales (Fairchild & Treble 2009). The mechanisms
59 by which these elements are incorporated vary depending on the physical properties of the element
60 (e.g. especially the charge and ionic radius – Bourdin et al. 2011), the carbonate mineral in question
61 (usually either calcite or aragonite, e.g. Balboni et al. 2015; Wassenburg et al. 2016, Chen et al.
62 2016) and the mineralization environment (e.g. marine vs cave vs soil; Mucci & Morse 1983;
63 Burton & Walter, 1991; Fairchild et al. 2000; Kelly et al. 2006). Key to understanding these
64 mechanisms and interpreting trace-element variations in palaeoenvironmental archives is the
65 quantification of the relationship between the trace element-to-calcium ratio $[X/Ca]$ of the
66 carbonate and that of the parent solution, known as the ‘partition coefficient’ $[D_X]$. This is defined
67 empirically as:

68

69
$$D_X = \frac{[X/Ca]_{CaCO_3}}{[X/Ca]_{aq}} \quad (1)$$

70

71 Speleothems (e.g. stalagmites, flowstones) are palaeoclimate archives composed of calcium
72 carbonate, usually in the form of the mineral calcite or aragonite (Fairchild & Baker 2012). They
73 are formed from carbonate-rich waters that have permeated through limestone or dolomite host rock.
74 When the waters reach an air-filled chamber with a lower partial pressure of carbon dioxide (PCO_2),
75 CO_2 outgassing causes the solution to become supersaturated with respect to calcite (or aragonite)
76 to a point where mineral precipitation occurs in the form of stalagmites, flowstones and other
77 speleothem types.

78

79 In the last two decades, speleothems have emerged as valuable palaeoenvironmental archives
80 because their source waters encode geochemical information on climate-driven shifts in rainfall,
81 temperature and/or vegetation above the cave (Fairchild & Baker 2012). Their utility is further
82 enhanced by the ability to date them accurately and precisely using U-Th and U-Pb methods (Cheng
83 et al. 2009, 2016; Woodhead et al., 2006), which allows the assembly of high-quality palaeoclimate
84 proxy time series.

85

86 The most widely used environmental proxies in speleothem studies are stable oxygen and carbon
87 isotope ratios (expressed as $\delta^{18}O$ and $\delta^{13}C$, respectively) (Fairchild & Baker 2012). Changes in
88 speleothem $\delta^{18}O$ are a function of the temperature of mineralisation in the cave and drip-water $\delta^{18}O$
89 (Hendy & Wilson 1968; Schwarcz et al. 1976), with the latter generally regarded as the main
90 driving factor (McDermott 2004; Lachniet 2009). Mean drip-water $\delta^{18}O$ values principally reflect

91 the amount-weighted average of $\delta^{18}\text{O}$ of effective recharge at a cave site, which can be affected by
92 seasonal changes in local hydrology (e.g. Markowska et al. 2016). The climate mechanisms
93 controlling local rainfall $\delta^{18}\text{O}$ reflect a complex series of fractionation processes that take place
94 between the original moisture source and the cave site (Lachniet 2009). Interpreting trends in
95 speleothem $\delta^{18}\text{O}$ in terms of changes in, for example, rainfall amount, dominant air-mass
96 trajectories and seasonality, can be challenging. The interpretation of speleothem $\delta^{13}\text{C}$ is similarly
97 complex (Lauritzen & Lundberg 1999; McDermott 2004), particularly in determining the relative
98 importance of climate-driven processes in the soil/epikarst and those occurring within the cave
99 chamber (which may or may not be climate-driven) (Fairchild & Baker 2012). Thus,
100 complementary sources of proxy information from alternative speleothem properties are useful for
101 refining palaeoclimate reconstructions.

102

103 Trace-element geochemistry has emerged as the principal means by which to extract such
104 complementary information (Johnson et al. 2006; Fairchild & Treble 2009; Griffiths et al. 2010;
105 Fairchild & Baker 2012; Fohlmeister et al. 2012; Hartmann et al. 2013; Orland et al. 2014). Trace
106 elements are sourced from aerosols, soils, vegetation, bedrock and/or sediment infills, and reach the
107 growing speleothem as colloids, solutes or particulates (Fairchild & Treble 2009). Although a wide
108 variety of elements has been investigated (Borsato et al. 2007; Zhou et al. 2008; Fairchild & Baker
109 2012; Day & Henderson 2013), most attention has been directed at elements that substitute for the
110 calcium ion (Ca^{2+}) in the crystal structure, notably Mg^{2+} , Sr^{2+} and Ba^{2+} (Mucci & Morse 1983;
111 Paquette & Reeder 1995; Rimstidt et al. 1998). Such elements are often sensitive to climate-driven
112 changes in cave hydrology (Fairchild & Treble 2009; Day & Henderson 2013; Tremaine et al.
113 2013), and thus have considerable value in refining or reinforcing interpretations of stable isotope
114 changes (Treble et al. 2005; Drysdale et al. 2006; Cruz et al. 2007; Liu et al. 2013; Wong et al. 2015;
115 Ünal-Imer et al. 2016; Bernal et al. 2016). This can be further complemented by data from other
116 isotope systems (e.g. Ca and U isotopes – Owen et al. 2016; Hellstrom & McCulloch 2000;
117 Drysdale et al. 2005).

118

119 A number of previous studies have determined partition coefficients directly using natural cave
120 waters and speleothems (Gascoyne 1983; Fairchild et al. 2001; Tremaine & Froelich 2013;
121 Wassenburg et al. 2016) and through laboratory ‘cave-analogue’ experiments (Huang & Fairchild
122 2001; Day & Henderson 2013), but their number is few owing to the practical difficulties of
123 farming calcite in caves and mimicking the intricate physico-chemistry of caves in a laboratory
124 setting. The great majority of the research conducted to date has been aimed largely at partitioning

125 between drip-waters and stalagmites (or analogues thereof), whereas partitioning into other
126 speleothem types remains largely unexplored.

127

128 In this study we investigate the partitioning of trace elements into subaqueous speleothem calcite.
129 Subaqueous speleothems have rarely been considered in palaeoenvironmental research. Most
130 speleothem studies to date have been based on either stalagmites or flowstones, which usually yield
131 higher-resolution records. However, the partitioning of trace elements into these stalagmites or
132 flowstones is likely to differ from that of subaqueous speleothems because of the strong contrast in
133 physico-chemical conditions, which govern reaction kinetics and, by implication, trace-element
134 partitioning (Fairchild & Baker 2012). Whilst subaqueous speleothems have been shown to be
135 potentially susceptible to radiometric dating problems (Edwards et al. 1993; Moseley et al. 2016),
136 their great value lies in their ability to capture long, continuous palaeoclimate records (Winograd et
137 al. 1992; Drysdale et al. 2012). Being mostly fed by multiple, rather than single, points of vadose
138 percolation flux, pool-water geochemistry is likely to be more representative of a regional response
139 to environmental change than stalagmites because, provided the pool is large enough, it potentially
140 integrates recharge from a larger surface above the cave and is less susceptible to the nuances of an
141 individual drip-water flow path. Here we present results from a series of near-monthly water
142 chemistry measurements from an Italian cave pool conducted over the period from May 2009 to
143 March 2012. We assess the temporal patterns of hydrochemical changes in the pool and compare
144 with the observed rainfall for the same period, then combine the pool-water and subaqueous calcite
145 [X/Ca] to calculate a series of partition coefficients (D_{Mg} , D_{Sr} , D_{Ba} and D_U). We then compare these
146 new data with published partition coefficients from mostly cave and cave-analogue studies.

147

148 2. STUDY SITE AND SAMPLING

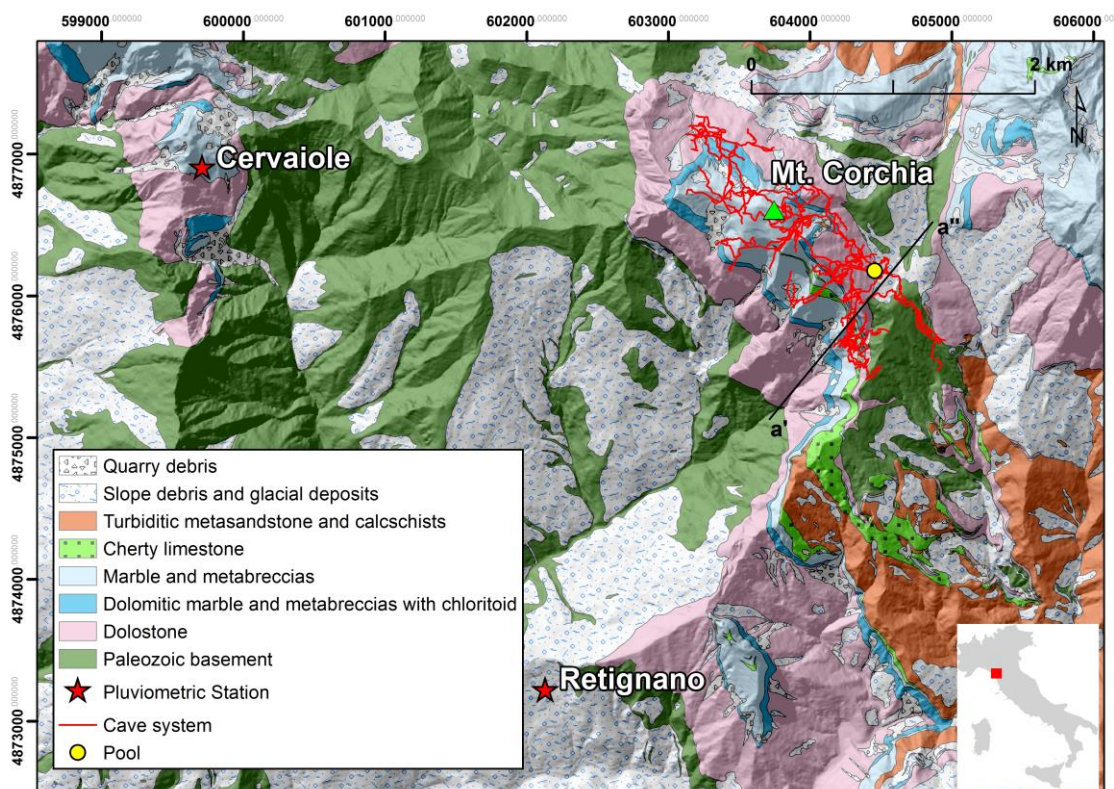
149 The water and calcite samples used in this study were collected from Antro del Corchia, a large
150 cave system developed in Mesozoic dolomites, marbles and dolomitic marbles of the Alpi Apuane
151 of western-central Italy (Piccini et al. 2008; Baneschi et al. 2011) (**Fig. 1**). The samples come from
152 a cave pool ('Laghetto Basso') (**Fig. 2 & 3**) that has developed on the floor of a large, well-
153 decorated chamber called the Galleria delle Stalattiti (GdS). The chamber is situated ~400 m
154 vertically below the surface at ~835 m above sea level, and is located about 1 km from the nearest
155 natural entrance to the cave (Piccini et al., 2008). The microclimate is relatively stable, typical of
156 deep-cave environments: based on continuous monitoring between 2002 and 2006, the mean (± 1
157 s.d.) temperature, wind speed and relative humidity of the chamber is 8.4 (0.3) °C, 0.09 (0.07) m s⁻¹,
158 and 100.0 (0.2) %, respectively (Piccini et al. 2008). Rainfall reaching the cave is derived primarily
159 from air masses moving eastwards from the North Atlantic (Drysdale et al. 2004). The Alpi Apuane

160 massif presents a topographic barrier to these air masses, and the orographic rainfall it promotes
161 produces an annual average of over 3000 mm at the watershed near Monte Corchia (Piccini et al.
162 2008).

163

164 The rock sequence above the GdS has been subjected to multiple phases of metamorphism
165 (Carmignani & Kligfield 1990; Kligfield et al. 1986). The Paleozoic basement, consisting mainly of
166 phyllites (Filladi Inferiori), porphyritic meta-volcanics (Porfiroidi e Scisti Porfirici), quartzites
167 (Filladi Superiori) and local lenses of graphitic schist and meta-dolostone (Dolomie a Orthoceras),
168 is overlain by the dolomitic ‘Grezzoni’, which is the basal portion of the metamorphosed Apuane
169 carbonates (**Fig. 2; Table A1**) (Carmignani & Giglia 1984; Conti et al. 1993). The Grezzoni has
170 been overfolded such that the basement sits topographically above the carbonates and is exposed at
171 the surface directly above the GdS chamber. However, whilst percolation waters almost certainly
172 enter the karst along the basement-dolomite contact, surface hydrography precludes significant
173 karst recharge via direct surface runoff from the basement itself (**Fig. 2**).

174



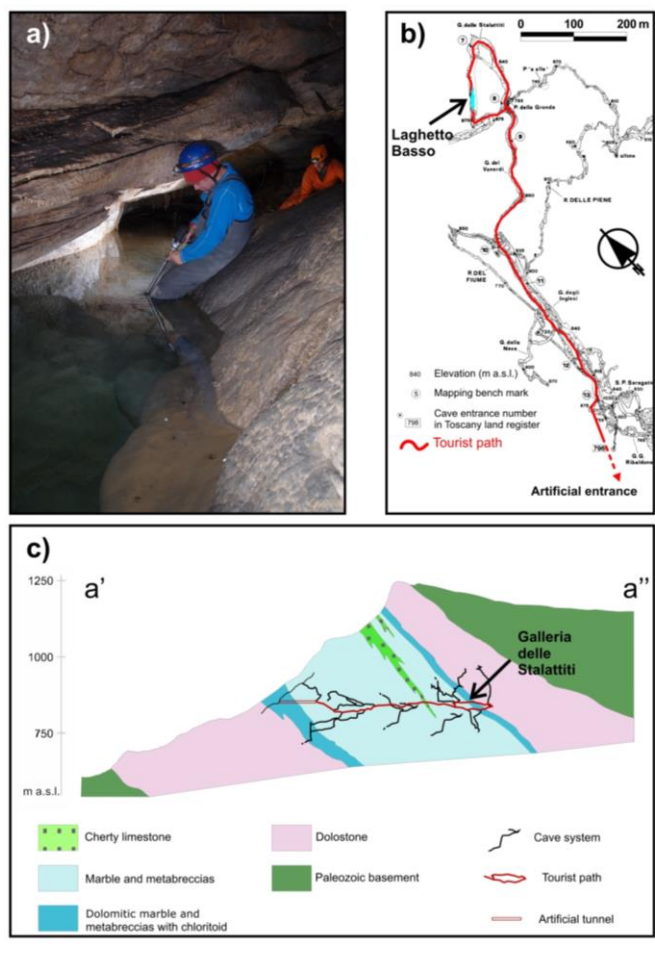
175

176 **Figure 1:** Location and geology of the study area. A geological cross section between a' and a'' is shown
177 in Figure 2c.

178

179 Based on a preliminary cave survey conducted in May 2017, the minimum volume of Laghetto
180 Basso has been calculated at 15.2 m³, 80% of which is contained within a single basin (**Fig. 3**). This
181 basin is fed largely by a drapery of stalactites that have grown from percolation waters issuing from

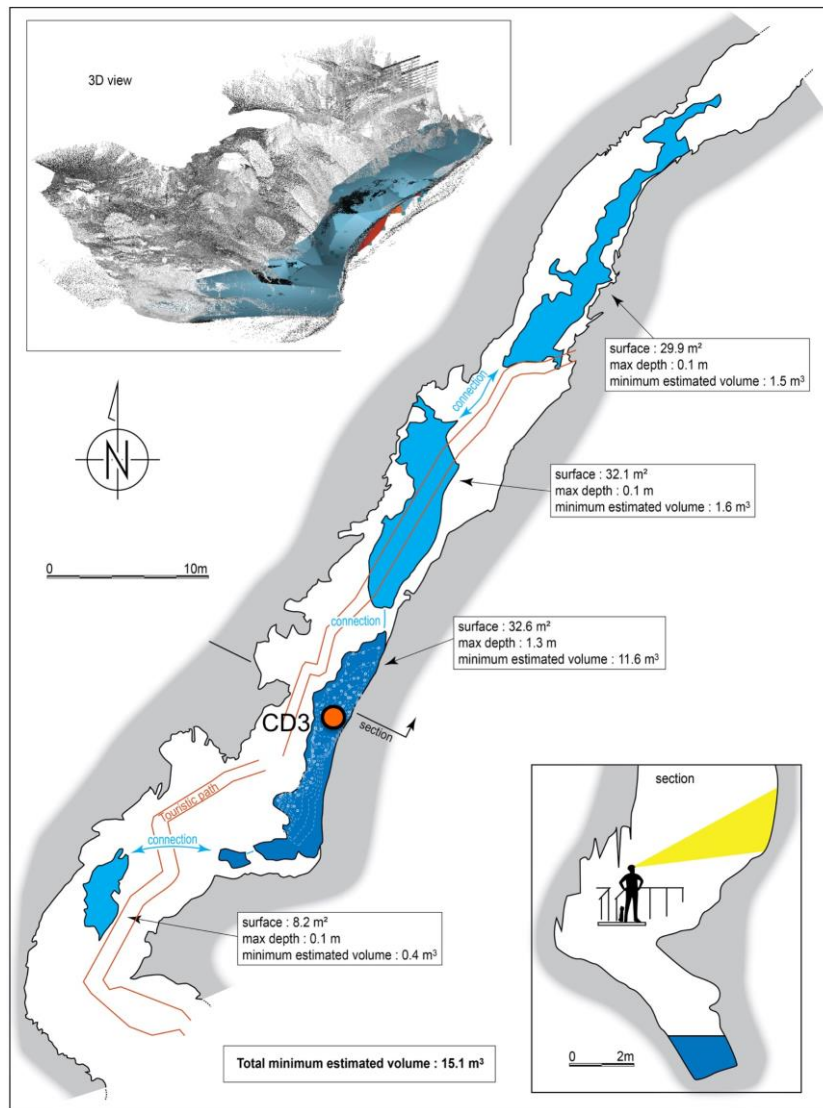
182 fractures aligned parallel to the strike of the carbonate beds that form the chamber's ceiling. It
 183 drains across a narrow sill at the southern end (Drysdale et al. 2012). Drip-water discharge
 184 monitoring at nearby site CNR2, conducted over a two-year period starting in October 2007,
 185 suggests relatively constant dripping rates (varying by less than ~50% around a mean value of 89
 186 drips per hour: Baneschi et al. 2011), suggesting some degree of dampening of seasonal recharge
 187 variations due to the long flow path and volume of vadose storage. One-off instantaneous drip
 188 measurements conducted in May 2017 showed that the pool receives at least ~37 L/day, equivalent
 189 to a mean residence time of the pool waters of almost one year. Based on the CNR2 drip-rate data,
 190 the month of May is a good proxy for mean annual drip rate (mean value: 93 drips per hour; May
 191 2008 and 2009 mean value: 95 drips per hour), suggesting the instantaneous pool measurements
 192 offer a reasonable first-order estimate of turnover rate. Stable isotope data show that the pool waters
 193 are isotopically very stable (Piccini et al. 2008; Baneschi et al. 2011; Daëron et al. 2019),
 194 suggesting the percolation waters are well mixed by the time they arrive in the pool.
 195



196
 197
 198
 199
 200
 201

Figure 2: (a) Laghetto Basso pool, from where the CD3 core was drilled. (b) Plan-view map of the part of Corchia Cave where this study was carried out. Galleria delle Stalattiti is located in the far north. (c) Topographic and geological cross section through Monte Corchia along a traverse (shown in Figure 1) incorporating the Galleria delle Stalattiti.

202 The wetted perimeter of Laghetto Basso is coated with a continuous crust of “mammillary calcite”
203 of variable thickness, similar to the well-known subaqueous vein calcite of Devils Hole, Nevada
204 (e.g. Winograd et al., 1992; Kolesar and Riggs, 2004). The crust morphology varies according to
205 that of the underlying bedrock floor, which is, in parts, littered with broken speleothems. In the
206 largest basin of Laghetto Basso, several ~hemispheric domes occur, from one (CD3) of which the
207 core sample (CD3-12) for this study was drilled (**Fig. 2**).
208



209
210 **Figure 3:** Plan and section view of Laghetto Basso derived from a 3D cave survey
211 conducted in May 2017. Volumetric data are shown for the individual basins. The basin
212 hosting the subaqueous speleothem CD3 is the largest.
213

214
215 **3. METHODS**

216 **3.1 Water sampling and analysis**

217 Water temperature, electrical conductivity (EC) and pH were measured directly in the Laghetto
218 Basso water using a portable multi-parameter meter (Delta OHM Instruments). Accuracy is 0.5%

219 for conductivity, 0.25% for temperature and 0.1 for pH. The pH and EC sensors were calibrated
220 prior to each sampling trip with certified standard buffer solutions (pH 4 and 7 solutions, and 147,
221 717.5 and 1413 $\mu\text{S cm}^{-1}$ solutions).

222

223 Total alkalinity was measured in the field within 1-2 hours of sampling by HCl (0.1 N) titration
224 according to Gran's method (Gran 1952) using methyl-orange as the indicator solution. The error of
225 the analysis is 0.01 meq L^{-1} . Additional samples were stored in chemically inert polyethylene
226 bottles with a screw cap and a separate internal closure plug for additional air-tight sealing. One
227 aliquot of each was filtered through a 0.45- μm cellulose-acetate syringe filter then split into two
228 acid-washed/MQ water-rinsed bottles: the first was acidified with suprapur HNO_3 (2% v/v,
229 TraceSELECT Fluka, with U, Ba, Sr < 0.5 $\mu\text{g/kg}$) for U, Sr and Ba analysis, whilst the second
230 fraction, reserved for cation Ca and Mg analysis, was acidified with HCl (2% v/v, Sigma-Aldrich
231 puriss. p.a. with Ca < 0.5 and Mg < 0.1 mg/kg) in order to prevent any post-sampling calcite
232 precipitation. A second unacidified aliquot was analysed for anions and Na. A "blank" sample
233 (MQ-water filtered and acidified in the field) was prepared to check for contamination during
234 sampling. All solutions were kept refrigerated at 4 $^{\circ}\text{C}$ until analysis.

235

236 Major cations (Ca, Mg and Na) were analysed by atomic absorption spectrometry (Perkin-Elmer
237 model 3110), and anions by ion chromatography (Dionex-100). The minor elements Sr and Ba were
238 measured by inductively coupled plasma atomic emission spectrometry (ICP-AES, Perkin-Elmer
239 Optima 200DV) at the Institute of Geoscience and Earth Resources, Consiglio Nazionale delle
240 Ricerche (CNR), Pisa, Italy. Uranium analysis was carried out using inductively coupled plasma
241 mass spectrometry (ICP-MS Perkin Elmer model ELAN 5000) at the EUROLAB laboratories in
242 Nichelino, Italy.

243

244 The analytical reproducibility (\pm) for Ca, Mg, Na, K, Cl and SO_4 was $\leq 2\%$, and $\leq 5\%$ for Sr, Ba, and
245 U. The detection limit for Ba and Sr was 1 ppb and for U was 0.5 ppb; these elements were
246 analysed on undiluted subsamples. All analyses included replicates, blanks and quality-control
247 standards measured with every set of unknown samples, the concentrations of which were
248 calculated from daily calibration curves. The calcite saturation indices (defined as the log of the
249 quotient of ionic activity product and solubility product) and the partial pressure of CO_2 in
250 equilibrium with the solution, expressed as $\log\text{PCO}_2$, were determined from the measured drip-
251 water chemistry using SOLVEQ (Reed 1982).

252

253 **3.2 Speleothem sampling**

254 Modern samples were obtained from the outer surface of drill core CD3-12, which was recovered
255 from CD3, a ~30-cm-high subaqueous dome-shaped mound, in December 2012 using a battery-
256 powered drill fitted with a 45-mm-internal-diameter, diamond-crowned core barrel (Spötl and
257 Matthey 2012). The core measures 260 mm in length and was drilled to bedrock. It was cut
258 longitudinally into two halves which were then polished. The speleothem bears no visible signs of
259 alteration and, like other cores drilled from the same pool (Drysdale et al., 2012), comprises a
260 compact crystalline calcite fabric of a predominantly columnar-fascicular optic type (*sensu* Neuser
261 & Richter 2007; Frisia 2015), with large polycrystals up to several centimetres long (length-to-
262 width ratio commonly > 10:1), oriented roughly perpendicular to the growth surface, and
263 characterised by undulatory extinction (in cross-polarized light). This fabric is common to
264 speleothems with a relatively high Mg content (typically from 10,000 to 30,000 ppm). In
265 stalagmites and flowstones, this has been shown to most likely develop where source-water Mg/Ca
266 lies between ~0.4 and ~3 mol/mol and where the calcite saturation index (SI_c) is between ~0.3 and
267 ~0.5 (Frisia 2015).

268

269 Each half of CD3-12 was ultrasonically cleaned in double-deionised water to remove any loose
270 particles that might be present on the active growth surface. It was then clamped face down to the
271 edge of a bolting plate fitted to the moving stage of a milling lathe (**Fig. A1**). Fifteen surface
272 carbonate samples (7 from one half, 8 from the other, giving a total of 15 aliquots) were then
273 carefully abraded individually from discrete ca. 1 cm² regions of the active outer growth surface
274 using a Dremel hand tool fitted with a 0.4-mm diameter diamond bur with the assistance of a 3x
275 magnification lense. A single pass across each crystal was made, and, using the bur diameter as a
276 guide, the depth of abrasion was conservatively estimated to be no more than 100 μm. The
277 carbonate was collected on weighing paper suspended on a scissor jack positioned beneath the
278 speleothem tip (**Fig. A1**). After sampling over each region, the core section was unclamped, and the
279 remaining powder transferred to the weighing paper by tapping the section. The yield was placed
280 into a clean 1.5 mL microcentrifuge tube. Prior to sampling the next region, the section was cleaned
281 using compressed air.

282

283 The yield from each region was split into several fractions for a range of analyses (including
284 clumped isotopes: Daëron et al. 2019). Two aliquots of ~0.2 – 1.0 mg were set aside for trace
285 element analyses by ICP-MS in two different laboratories: the Isotope Geochemistry Laboratory at
286 the School of Earth Sciences, The University of Melbourne (herein ‘UM’), and the Elemental
287 Laboratory, Isotope Tracing in Natural Systems, the Australian Nuclear Science and Technology
288 Organisation (herein ‘ANSTO’).

289

290 3.3 Speleothem age

291 Exploratory uranium-series dating of CD3 suggested a basal age of around 1 Ma (Drysdale et al.
292 2008). This has been confirmed by comparing stable isotope profiles from Corchia Cave
293 stalagmites dated by U-Pb, including stalagmite CC8 reported in Bajo et al. (2012), with isotope
294 profiles from the base of CD3 (our unpublished data). Ages reported in Drysdale et al. (2012) from
295 core CD3-1 (drilled in 2007; length: 260 mm), covering the depth range of ~40 to ~50 mm from the
296 top, span 229 ± 5 to 295 ± 8 ka, consistent with a basal age of the order of 1 Ma. Verifying a ‘modern’
297 age at the top of CD3, on the other hand, has proved somewhat more challenging. U-Th
298 measurements on powders carefully scraped from the very outer surface give ages up to several
299 thousand years before present, suggesting growth had stopped well before the monitoring period for
300 this study. However, a subsequent chronology (**Table A2**) used to anchor CD3 $\delta^{18}\text{O}$ and $\delta^{13}\text{C}$ time
301 series reveals that stable isotope patterns are up to several thousand years older than those from a
302 well-dated coeval stalagmite (CC26) (Zanchetta et al. 2007; Bajo et al. 2016; see supplementary
303 information in **Appendix 1** and **Fig. A2 to A6**). This indicates that CD3 yields older-than-true ages,
304 and that the pool water is susceptible to the same dating issue recently proposed for Devils Hole
305 (Nevada, USA): the growing surface of subaqueous calcite scavenges excess ^{230}Th produced by
306 decay of ^{234}U in the water column (Edwards & Gallup 1993; Moseley et al. 2016). To place CD3
307 onto an accurate age scale and to quantify the age offset, we synchronised its $\delta^{18}\text{O}$ and $\delta^{13}\text{C}$ profiles
308 to those of CC26 (**Fig. A5**). The results show that the mean offset over the Holocene is ~2 kyr. The
309 $\delta^{18}\text{O}$ and $\delta^{13}\text{C}$ at the top of CD3 (Daëron et al. 2019) is consistent with the $\delta^{18}\text{O}$ and $\delta^{13}\text{C}$
310 composition of the tips of stalagmites actively growing within a 20 m radius of the pool (**Fig. A5**).
311 Therefore, whilst we cannot definitively demonstrate that CD3 is active today due to its slow
312 growth rate and the incorrect U-Th dates, the combined evidence of: (i) the corrected CD3 age
313 profile; (ii) the excellent agreement between the isotopic composition of the CD3 outer surface and
314 that of actively growing stalagmites near the pool; and (iii) the fact that the speleothem has grown
315 continuously over almost the last million years, including glacial periods (Drysdale et al. 2012),
316 would indicate that the speleothem is actively growing today. We also note that the slow growth
317 rate precludes the detection of the radiocarbon bomb pulse, as has been possible for faster-growing
318 speleothems (Genty & Massault 1997; Matthey et al. 2008; Hodge et al. 2011; Griffiths et al. 2012).
319

320 Based on the thickness of its Holocene section (~4 mm; **Fig. A6**), and the likelihood of relatively
321 stable growth rates based on previously studied Holocene stalagmites from Corchia (Zanchetta et al.
322 2007; Bajo et al. 2016; Isola et al. 2019), the sampled surface calcite of CD3-12 conservatively
323 integrates the last ~300 yr of growth.

324

325 **3.4 Calcite analyses**

326 *3.4.1 Solution analyses of CD3-12 core-top calcite*

327 For solution analyses at UM, the calcite aliquots were dissolved in 1 mL of 5% twice-distilled
328 HNO₃ containing a nominal 2 ppb of internal standards (⁶Li, ⁸⁴Sr, ²³⁵U and In). The vial contents
329 were mixed by shaking then dispensed into tubes for analysis. A further 1 mL was added to the
330 now-empty vials and the process repeated to ensure all solutes were removed. For the purpose of
331 preparing standards, data from previous laser-ablation ICP-MS analyses on Laghetto Basso calcite
332 enabled the matrix of the speleothem to be matched as closely as possible. A 50:50 mix of a
333 previously analysed speleothem solution and a basalt rock standard solution were used for
334 calibration for a better matrix match than the pure silicate rock standards normally used for
335 calibration. Samples were run on an Agilent 7700x ICP-MS. The calibration standard was run every
336 8 samples to correct for external drift after internal standard normalisation.

337

338 At ANSTO, the aliquots were digested in 3% Merck suprapur HNO₃ which was spiked with an
339 internal standard to a final concentration of 20 ppb. Standards were prepared using the same spiked
340 3% HNO₃ solution. The standard concentrations were prepared according to previously determined
341 approximate sample concentrations. The elements were analysed using a Varian 820MS ICP-MS
342 with internal standards used to correct for matrix effects and instrument drift. Standard checks were
343 analysed after every 20th sample.

344

345 In both laboratories, elements were normalized to ⁴³Ca and molar ratios calculated. The
346 reproducibility for the calibration standard ratios at UM were 1.2% for (²⁵Mg:⁴³Ca), 1.0% for
347 (⁸⁸Sr:⁴³Ca), 1.0% for (¹³⁷Ba:⁴³Ca), and 0.9% for (²³⁸U:⁴³Ca), whilst at ANSTO they were 1.6% for
348 (²⁵Mg:⁴³Ca), 1.6% for (⁸⁸Sr:⁴³Ca), 1.2% for (¹³⁷Ba:⁴³Ca), and 1.3% for (²³⁸U:⁴³Ca).

349

350 *3.4.2 Laser-ablation analyses of the outermost layer of CD3-12 calcite*

351 To complement the calcite solution ICP-MS analyses, we used laser-ablation inductively coupled
352 plasma mass spectrometry (LA-ICP-MS) to investigate the level of homogeneity of Mg, Sr, Ba and
353 U concentrations in the outermost layer of CD3-12 (**Fig. A7**). To achieve this, analyses were
354 conducted on a polished section of CD3-12 using a 193-nm Ar-F excimer laser-ablation system
355 coupled to an Agilent 7700x quadrupole ICP-MS. The laser targetted the outermost 7 μm, running
356 parallel to the growth surface. The operating conditions of the laser and ICP-MS, as well as the
357 elements/masses that were analysed, are summarised in **Table 1**. The sample was first ultra-
358 sonically cleaned in double-deionised water for 15 minutes then fitted into the sample holder of the

359 laser system, which moves in x , y via a computerised stage. The RESOLUTION laser-ablation system,
360 fitted with a Laurin Technic two-volume ablation cell, is driven by *GeoStar* software (Resonetics)
361 and was set up to ablate seven traverses of unequal length along the outermost 7 μm (e.g.
362 Woodhead et al., 2007) (**Fig. A7**) and using a 7- μm -square ablation profile. Based on a mean
363 Holocene growth rate of $\sim 0.34 \mu\text{m yr}^{-1}$ (Appendix 1), this is likely to integrate the last ~ 21 years of
364 growth up to the date of core drilling (December 2012), encompassing the period over which the
365 water sampling was conducted. Although the accuracy and precision of the calcite LA-ICP-MS
366 results are unlikely to compete with those from the solution analyses due to the lack of a compatible
367 matrix-matched standard against which to calibrate raw laser data, the advantage lies in its
368 outstanding spatial detail. The technique should resolve significant changes in element
369 concentrations that might be related to, for example, the mode of element incorporation (e.g.
370 replacement, interstitial) or crystal zoning (Reeder & Grams 1987).

371
372 Each ablation ‘spot’ ($n=120$ in total) was ablated for 15 s at a pulse rate of 5 Hz and a fluence of 5 J
373 cm^{-2} . The spacing between successive ablation centres was 8 μm . Ablation took place in an
374 environment of ultra-high-purity helium, with the ablated aerosol carried into the mass spectrometer
375 under an ultra-high-purity argon stream. Elemental concentrations were calibrated against the NIST
376 SRM610 glass reference standard (measured three times during the session) with ^{43}Ca used as an
377 internal standard to monitor and correct for instrument drift. Raw mass spectrometry data were
378 reduced using *Iolite* software (Hellstrom et al., 2008; Paton et al., 2011). A laser log file produced
379 by *GeoStar* records the laser state and the position of the laser spot against a timestamp. For each
380 spot, the first 2 s were cropped to eliminate residual surface contaminants after ultrasonication,
381 whilst the last 8 s were cropped due to down-hole diminution of yield and mass fractionation. This
382 resulted in a final data acquisition time of ~ 5 s per spot, equivalent to 24 or 25 data points per spot.
383 The mean analytical uncertainty on the four elements based on the internal 95% standard error (2
384 s.e.) on the three NIST610 glass standard measurements is between 3.0 and 3.8%.

385
386 Finally, the mean and standard deviation from the LA-ICP-MS Mg, Sr, Ba and U data were
387 calculated and combined with the pool water $[\text{X}/\text{Ca}]$ to derive a comparison series of D_{X} values.

388

389 **3.5 Rainfall data**

390 To determine the sensitivity of pool-water trace element concentrations to cave recharge, hourly
391 pluviometric data from the nearest rain gauging stations (Cervaiolo: ~ 4.5 km WNW of Monte
392 Corchia, elevation 1140 m a.s.l.) and Retignano (~ 3 km SSW of the cave entrance, 440 m a.s.l.) (**Fig.**
393 **1 & 2**) were aggregated to produce monthly series over the period of water sampling.

394

395

396 **4. RESULTS**

397 **4.1 Pool-water chemistry**

398 The pool-water chemistry of Laghetto Basso is summarised in **Table 2**; additional data, including
399 charge balances, saturation indices and PCO_2 values, are contained in **Table A3**. The Laghetto
400 Basso water temperature is stable at $7.9 \pm 0.4^\circ\text{C}$ (2σ), which is to be expected from a deep-
401 interior chamber. The pH of the waters is slightly alkaline, and for most of the sampling period
402 only fluctuated within a narrow envelope (± 0.2 units). The ion chemistry indicates that the waters
403 are of low ionic strength for a karstic environment (Drysdale 2001; McDonald et al. 2007;
404 Tremaine & Froelich 2013). The Mg^{2+} concentrations are relatively high, and yield $[\text{Mg}/\text{Ca}]$
405 persistently above 1 (mean ± 1 s.d. 1.18 ± 0.06). The mean concentrations of Sr ($56.0 \pm 3.5 \mu\text{g L}^{-1}$)
406 and Ba ($23.8 \pm 2.1 \mu\text{g L}^{-1}$) produce $[\text{Sr}/\text{Ca}]$ and $[\text{Ba}/\text{Ca}]$ ($0.88 \pm 0.11 \text{ mmol mol}^{-1}$ and 0.24 ± 0.04
407 mmol mol^{-1}) that are significantly ($\sim 3x$) enriched compared to the Grezzoni dolomite bedrock
408 $[\text{Sr}/\text{Ca}]$ and $[\text{Ba}/\text{Ca}]$ values ($0.29 \text{ mmol mol}^{-1}$ and $0.07 \text{ mmol mol}^{-1}$ respectively (Azzaro et al. 1987;
409 Cortecci et al 1999; **Table A1**). Sulphate is also present at moderate concentrations (up to $\sim 32 \text{ mg}$
410 L^{-1} ; **Table A3**). Pool-water PCO_2 averages around twice that of the open atmosphere, whilst mean
411 calcite saturation is $\sim 0.27 \pm 0.18$ (2σ).

412

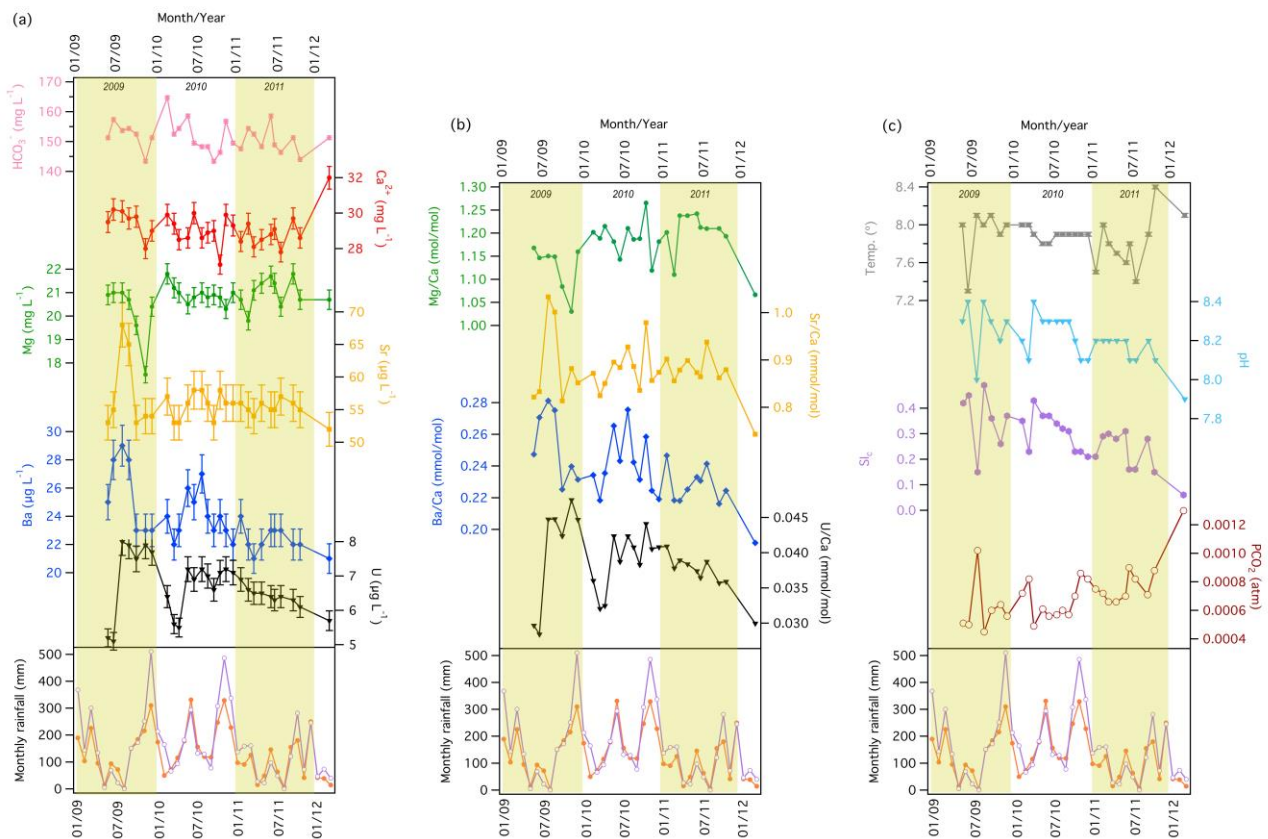
413 The concentration of each ion is relatively invariant, with coefficients of variation (CVs, based on
414 2σ) less than 10% for all species; the CVs of the major elements Ca^{2+} , Mg^{2+} and HCO_3^- are less
415 than 4% (**Table 2**). A consequence of the \sim invariant ion concentrations is stable $[\text{X}/\text{Ca}]$, with mean
416 and 2σ uncertainties for $[\text{Mg}/\text{Ca}]$, $[\text{Sr}/\text{Ca}]$, $[\text{Ba}/\text{Ca}]$ and $[\text{U}/\text{Ca}]$ being 1.175 ± 0.055 (mol/mol),
417 0.879 ± 0.058 (mmol/mol), 0.238 ± 0.021 (mmol/mol) and 0.039 ± 0.010 ($\mu\text{mol/mol}$) respectively
418 (**Table 2**). Such invariant solution chemistry and the availability of naturally accreted subaqueous
419 calcite indicates that Laghetto Basso is ideally suited for yielding well-constrained calcite partition
420 coefficients.

421

422 **4.2 Temporal patterns in pool-water chemistry and rainfall**

423 Plots of the major hydrochemistry parameters and the derived indices (PCO_2 and the calcite
424 saturation index, SI_c) against time are shown in **Fig. 4**. On first inspection, there does not appear to
425 be any patterns that would indicate clear, and mutually consistent, hydrologically driven changes
426 over the monitoring period (**Fig. 4**). Prominent peaks occur simultaneously in Sr^{2+} and Ba^{2+}
427 between July and August 2009; U concentrations rise around the same time but the peak persists
428 well after Sr^{2+} and Ba^{2+} fall, and the peaks are not consistently matched by other ions through the

429 same period. On the other hand, the decrease in Mg^{2+} shortly after (October 2009) is to some extent
 430 expressed in both Ca^{2+} and HCO_3^- , suggesting a dilution effect, but not in pH, PCO_2 or SI_c . If a
 431 dilution effect were responsible this should also impact Sr and Ba, but both of these ions are
 432 ~invariant through this interval. Overall, there is a suggestion of a weak downward trend in HCO_3^-
 433 and Ca^{2+} (if one ignores the last data point). Both Ba^{2+} and, particularly, U show a downward trend
 434 from late 2011; Sr^{2+} also shows a steady decrease from late 2011. These latter changes are
 435 proportionally greater than the subtle overall decreases in HCO_3^- and Ca^{2+} . The pH also tends to
 436 decrease through time but correlations with the downward trending ions are weak and statistically
 437 insignificant.



438
 439 **Figure 4:** Comparison of Laghetto Basso pool-water geochemistry and local rainfall amount through the monitoring
 440 period: (a) ion concentrations; (b) ion ratios; and (c) temperature, pH, PCO_2 and SI_c . Each lower panel shows the
 441 monthly rainfall amounts for two nearby rainfall gauging stations Cervaiolo (1140 m a.s.l., orange) and Retignano (440
 442 m a.s.l., purple). Vertical errors bars in panel (a) are 1 s.d. analytical uncertainties.

444 The monthly rainfall patterns for Cervaiolo and Retignano (**Fig. 4**) over the monitoring period
 445 broadly follow one another. Peaks occur in autumn to mid winter in all years, although conditions
 446 were wetter for 2009-10 and 2010-11 than in 2011-12, and the spring-to-early-summer peak in 2010
 447 is significantly higher than the corresponding periods for the years either side.

448 4.3 Calcite geochemistry

449 4.3.1 Solution ICP-MS data from calcite surface scrapings

451 The [X/Ca] ratios from the surface calcite of CD3-12 are shown in **Table 3**. The mean values from
452 both UM and ANSTO laboratories compare favourably within their respective 2σ uncertainties,
453 although there are some systematic offsets that imply analytical incongruencies between the two
454 sets of analyses. The mean [Mg/Ca] and [Ba/Ca] measured at UM are 1.3% and 7.3% higher than
455 those measured at ANSTO, respectively, whilst the mean [Sr/Ca] is 2.2% lower.

456

457 The degree of scatter in molar ratios amongst the 15 calcite samples is relatively small for [Mg/Ca],
458 [Sr/Ca] and [Ba/Ca], with CVs (based on 2σ) $\leq 3.3\%$ (**Table 3**); variability in [U/Ca], however, is
459 more than twice that for the other ratios.

460

461 *4.3.2 LA-ICP-MS analysis of calcite from the outermost $\sim 7 \mu\text{m}$*

462 **Table 4** and **Fig. 5** summarise the results of the LA-ICP-MS analyses of the outer rim of CD3-12;
463 the raw data from each spot along each of the seven traverses are shown in **Table A4**. The data
464 from each 5-s spot measurement yields a mean and 95% standard error for each of the four elements.
465 These standard errors provide an approximation of the analytical precision of the spot analysis,
466 assuming there is no significant downhole change in element concentrations, which is reasonable
467 because the $7 \mu\text{m} \times 7 \mu\text{m}$ laser profile reaches a depth of only $\sim 2.5 \mu\text{m}$ across the period of
468 ablation. The average standard error for each element based on the standard errors of all 120 spots
469 provides an estimate of the overall analytical uncertainty of the sample measurements. The standard
470 deviation from the mean values of all 120 spots for each element, on the other hand, indicates the
471 variability in each element's concentration across the outermost $7 \mu\text{m}$ of CD3-12, and thus provides
472 a measure by which to compare the variability in concentrations from the calcite solution ICP-MS
473 data in section 4.3.1.

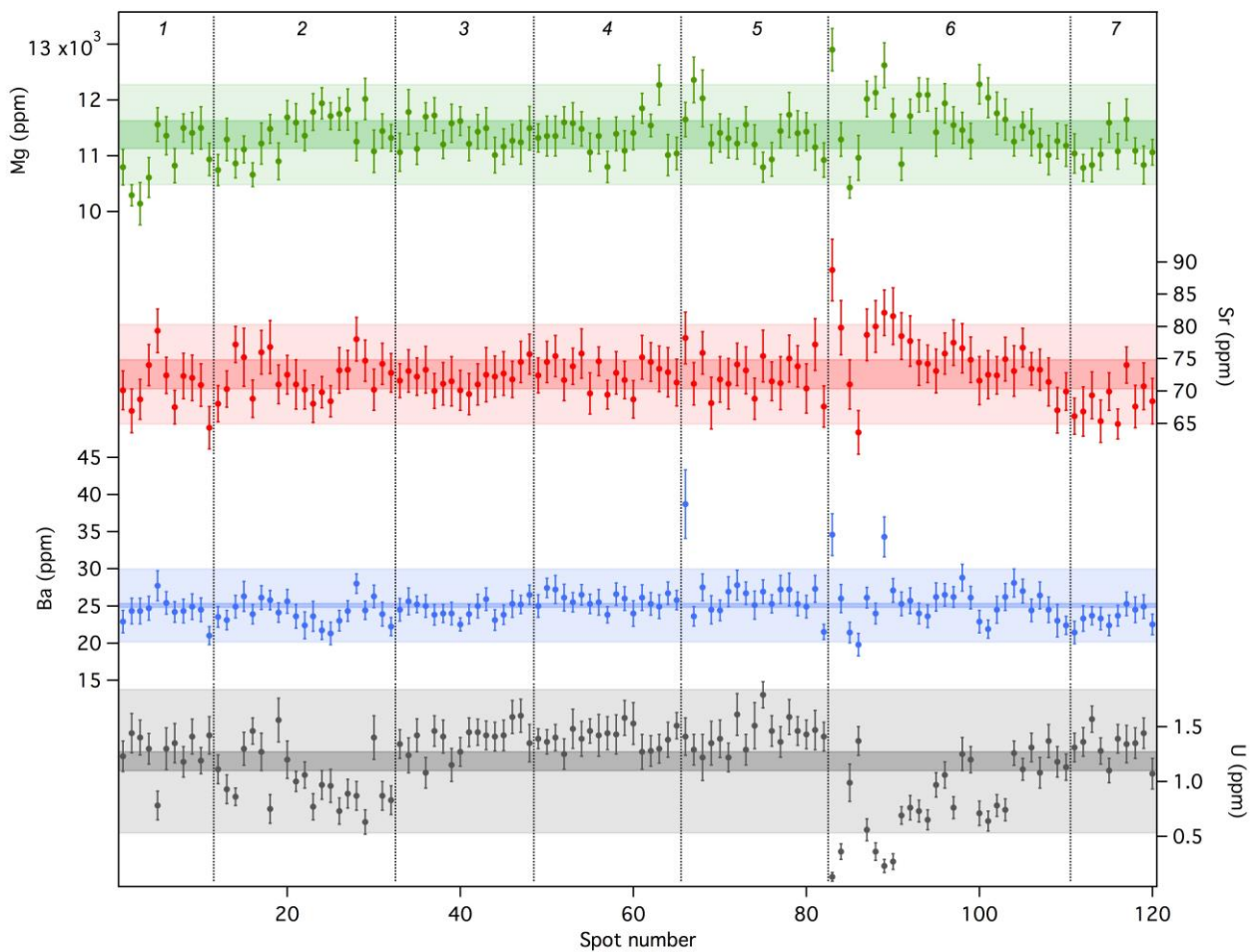
474

475 The overall variability in the laser data is higher than that for the solution data (**Table 4**), which is
476 to be expected given the higher resolution of the laser spot compared to the area ($\sim 1 \text{ cm}^2$) and
477 thickness (not exceeding $100 \mu\text{m}$) of the calcite sampled from the core top for the solution ICP-MS
478 analyses. The range of concentrations of each element measured by LA-ICP-MS is also well in
479 excess of the variability observed in the three NIST610 analyses (range 5.3% to 6.6%, 2 s.e.)
480 conducted before, during and after sample acquisition. Thus, the laser analyses appear to capture
481 real variability, both within and between most traverses. For example, all elements show variability
482 along traverses 2 and 6, whilst the variability across traverse 3 is minimal. Furthermore, the rank
483 order of variability for each element is similar in both analyses, with Mg having the least variability
484 and U having the greatest.

485

486 **4.4 Partition coefficients**

487 Partition coefficients (D_X) were derived by combining the UM and ANSTO CD3-12 solution trace
488 element datasets. We first applied the reduced χ -squared test (Reiners et al. 2017) to determine if
489 the UM and ANSTO calcite measurements for each element were drawn from the same population.
490 The calculated χ -squared statistic, or mean square weighted deviation (MSWD), is below the
491 critical value of χ for each of the paired [X/Ca] means at the 95% probability level, indicating that
492 each pair is drawn from the same population. Accordingly, error-weighted means were calculated
493 for each ratio along with their error-weighted 95% uncertainties (bottom panel of **Table 3**).
494 Applying equation (1) and combining the calcite and pool water [X/Ca] fractional uncertainties in
495 quadrature yields the mean $\pm 1\sigma$ partition coefficients for Mg, Sr, Ba and U shown in **Table 5**.
496 Partition coefficients are also shown for CD3-12 derived from the pool-water [X/Ca] and laser-
497 ablation [X/Ca] data from the outermost $\sim 7 \mu\text{m}$, with fractional uncertainties calculated in the same
498 way. The two sets of partition coefficients for CD3 are statistically indistinguishable, although the
499 uncertainty for the laser-derived measurements is larger.



500
501 **Figure 5:** LA-ICP-MS trace element results (Mg, Sr, Ba and U) based on seven discrete traverses (total number of spots:
502 120) along the outermost $7 \mu\text{m}$ of core CD3-12. Each data point represents the mean concentration based on a five-
503 second analysis window; the individual error bars are the 2 s.e. of measurement. The vertical lines separate the
504 individual traverses (numbered at the top; see Fig. A7 for the position of the traverse on the sample section). The
505 lighter-coloured bands are 2 s.d. envelopes around the mean of all laser spot values, as quoted in bold in the lower panel

506 of Table 4. To compare the variability between laser and solution data, the dark-coloured bands are the corresponding 2
507 s.d. envelopes for the averaged calcite solution-analysis results. These were derived by converting molar ratios to
508 elemental concentrations using the data in Table 3, and applying a Ca concentration of 39% (considering CD3 Mg
509 concentrations of ~1%). The dark-coloured bands were then centred on the LA-ICP-MS average for each element.
510

511

512 **5. DISCUSSION**

513 **5.1 Low ionic strength waters of Laghetto Basso**

514 The Laghetto Basso pool waters are of low ionic strength, with concentrations of major ions (Ca^{2+} ,
515 Mg^{2+} and HCO_3^-) being at the lower end of the spectrum of cave percolation waters. Part of the
516 reason for this is the likelihood of low PCO_2 of the infiltrating waters as they enter the karst, which
517 can be attributed to the low soil cover above the cave (Drysdale et al. 2004). Much of the surface
518 above Corchia Cave is steep and devoid of substantive soil cover. Here, the ground is criss-crossed
519 by fractures, which facilitates infiltration. This exposed, high-purity carbonate rock produces
520 negligible soil-forming insoluble residue. Instead, soils are confined either to lower-angle, largely
521 debris-mantled slopes to the northeast and comprise almost entirely organic matter, or to solution
522 features etched into the karst rock. The areas of greatest soil development above the cave occur on
523 the phyllite basement rock, which crops out on the eastern flank of Monte Corchia and is vertically
524 above the GdS. However, hydrographic constraints suggest that significant runoff from the
525 basement is unlikely to reach this part of the karst (**Fig. 2**). The low ionic strength and low calcite
526 saturation values of the pool waters (**Table A3**), and the subaqueous setting, are also undoubted
527 contributors to the excessively slow growth rates of CD3-12 (Drysdale et al. 2012). The slow
528 growth rates could also be influenced by the presence of relatively high $[\text{Mg}/\text{Ca}]$ and SO_4^{2-}
529 concentrations, which are known inhibitors of calcite crystal growth (Busenberg & Plummer 1989;
530 Nielsen et al. 2016).

531

532 The most distinguishing feature of the pool hydrochemistry, however, is its overall stability through
533 time when compared to cave waters reported in other studies (e.g. Fairchild et al. 2000; McDonald,
534 et al. 2004; Tremaine & Froelich 2013; Casteel & Banner 2015), including those where
535 measurements of pool waters have been made (Huang et al. 2001). This supports earlier assertions
536 of hydrochemical stability of Laghetto Basso (Piccini et al. 2008) based on lower-frequency
537 sampling between 1997 and 2006 (see summary in the lower panel of **Table 2**). This attests to the
538 very deep-seated position of Laghetto Basso within the cave system and its dampening effect on
539 hydrochemical variability.

540

541 The persistently high $[\text{Mg}/\text{Ca}]$ in the pool waters (**Table 2**) exceeds the ratio predicted from the
542 dissolution of the Grezzoni dolomite bedrock (Azzaro et al. 1987; Cortecci et al. 1999), suggesting

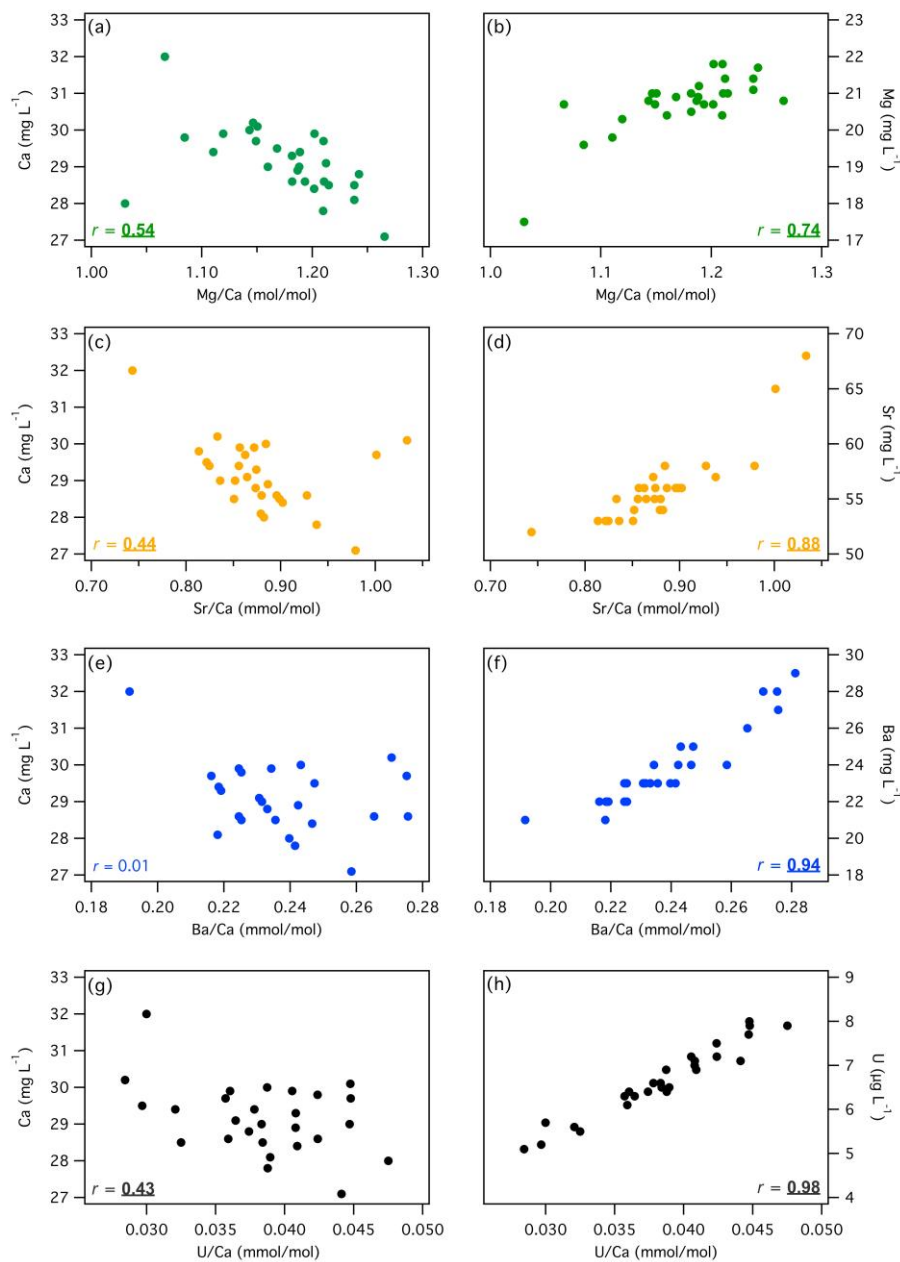
543 that prior calcite precipitation (PCP) (Fairchild et al. 2000; Bajo et al. (2017) and/or incongruent
544 dissolution of dolomite (Busenberg & Plummer 1982) are important processes controlling the
545 evolution of the percolation waters upstream of the pool. PCP occurs when calcite is precipitated
546 along the percolation-water flow path before it reaches the speleothem under study. This causes a
547 loss of Ca^{2+} from solution and an increase in the $[\text{X}/\text{Ca}]$ of the percolation water. The operation of
548 each of these processes can be tested using correlation. If PCP were important, Ca would decrease
549 as $[\text{Mg}/\text{Ca}]$ increases (Fairchild et al. 2000), whereas incongruent dissolution of dolomite, a
550 theoretically plausible process under the partially closed-system conditions that occur at Corchia
551 (Bajo et al. 2017), should produce a positive correlation between Mg and $[\text{Mg}/\text{Ca}]$ because Ca is
552 consumed by CaCO_3 precipitation as further Mg is released by continued dissolution of dolomite
553 according to the reaction:



557 and owing to the lower solubility of dolomite. On the other hand, PCP should not increase Mg
558 concentrations. For Ca vs $[\text{Mg}/\text{Ca}]$ and Mg vs $[\text{Mg}/\text{Ca}]$, both correlation coefficients are statistically
559 significant ($p < 0.05$; $df = 26$; one-tailed Pearson r), but the correlation for Mg vs $[\text{Mg}/\text{Ca}]$ is much
560 higher (Panels a-b, **Fig. 6**). The pattern is the same for $[\text{Sr}/\text{Ca}]$ and $[\text{U}/\text{Ca}]$: both pairs of r values are
561 statistically significant, but Sr vs $[\text{Sr}/\text{Ca}]$ and U vs $[\text{U}/\text{Ca}]$ (panels c-d and g-h, **Fig. 6**) are much
562 higher. For $[\text{Ba}/\text{Ca}]$, the correlation with Ca is almost zero, whilst the correlation with Ba is 0.94
563 (panels e-f, **Fig. 6**). As noted earlier, however, $[\text{Sr}/\text{Ca}]$ and $[\text{Ba}/\text{Ca}]$ are $\sim 3\text{x}$ enriched in the pool
564 waters compared to the Grezzoni bedrock (Azzaro et al. 1987; Cortecchi et al 1999; **Table A1**),
565 whereas $[\text{Mg}/\text{Ca}]$ are only $\sim 1.2\text{x}$ enriched. Both $[\text{Sr}/\text{Ca}]$ and $[\text{Ba}/\text{Ca}]$ are also significantly
566 correlated (Pearson's r correlation, $r = 0.71$, $df = 26$; $p < 0.05$; **Fig. 7**), suggesting enrichment from
567 a common source. If incongruent dissolution of dolomite were also contributing to enriched $[\text{Sr}/\text{Ca}]$
568 and $[\text{Ba}/\text{Ca}]$ we would expect both these ratios to be positively correlated with $[\text{Mg}/\text{Ca}]$, but this is
569 not the case (**Fig. 7**). Instead, the enriched $[\text{Sr}/\text{Ca}]$ and $[\text{Ba}/\text{Ca}]$ may be sourced where a component
570 of the infiltration waters exploits the contact between the Paleozoic basement rock and the Grezzoni.
571 This may explain the matching peaks in mid 2009 and decreasing trends from mid 2011 in both Sr^{2+}
572 and Ba^{2+} . The tendency for U to share some of the patterns of Sr^{2+} and Ba^{2+} suggests it is also partly
573 derived from a non-dolomitic source such as the basement rock.

574
575 The pool water contains moderate concentrations of SO_4^{2-} , which is likely sourced from pyrite that
576 is present throughout the Apuane metamorphosed carbonates (including the Grezzoni dolomite). An
577 alternative source is anhydrite, which, according to Azzaro et al. (1987), is present in the Grezzoni

578 sequence. However, this appears unlikely as it would also contribute more Ca^{2+} to the waters, and
 579 there is no excess Ca^{2+} in the pool-water chemistry. Weathering of pyrite can lead to sulphuric-acid
 580 dissolution of the carbonate host rock, and in a previous study (Bajo et al. 2017) from GdS mass-
 581 balance calculations indicate that such sulphuric-acid dissolution makes up one-third of the total
 582 dissolved carbonate content of waters, with the remainder derived from carbonic-acid dissolution
 583 involving soil CO_2 . Therefore, whilst the observed Ca^{2+} - Mg^{2+} - HCO_3^- concentrations are lower than
 584 is usually found in karst systems, they would be even lower were it not for a contribution from
 585 bedrock dissolution caused by sulphide weathering.
 586



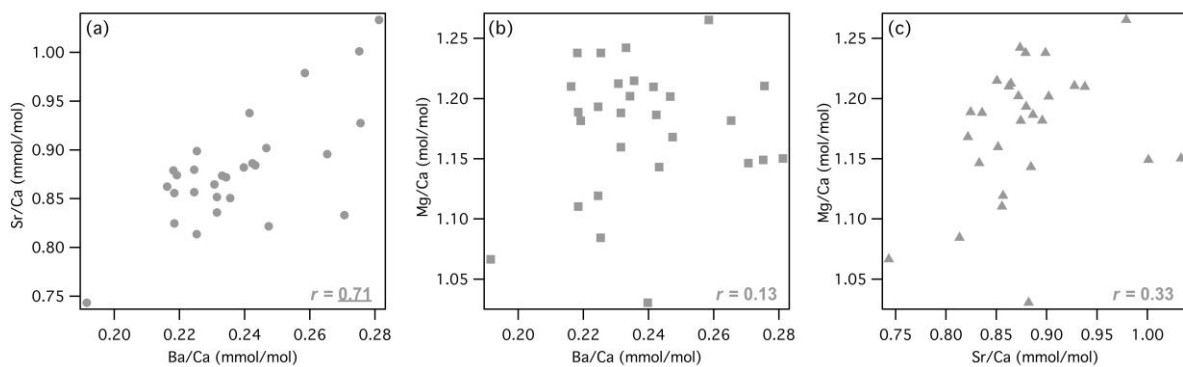
587
 588 **Figure 6:** Scatterplots between aqueous $[\text{X}/\text{Ca}]$ and their constituent ions for Laghetto Basso pool water. (a) Ca vs
 589 $[\text{Mg}/\text{Ca}]$; (b) Mg vs $[\text{Mg}/\text{Ca}]$; (c) Ca vs $[\text{Sr}/\text{Ca}]$; (d) Sr vs $[\text{Sr}/\text{Ca}]$; (e) Ca vs $[\text{Ba}/\text{Ca}]$; (f) Ba vs $[\text{Ba}/\text{Ca}]$; (g) Ca vs
 590 $[\text{U}/\text{Ca}]$; (h) U vs $[\text{U}/\text{Ca}]$. Pearson r correlation coefficients are shown (underlined values are statistically significant at p
 591 ≤ 0.05).
 592

593

594 5.2 Relationship between pool hydrochemistry and rainfall

595 The major hydrochemical parameters from Laghetto Basso show no clear and consistent
596 relationships with rainfall through the sampling period (**Fig. 4**) when compared with monthly
597 rainfall data from Cervaiolo and Retignano over the same period. We tested this by interpolating the
598 rainfall series to the calendar dates of water sample collection and calculating Pearson r correlation
599 coefficients between each ion and both rainfall series using lags between zero and 19 months (after
600 which $n < 10$). Most r values are below 0.1 and only one significant correlation emerges: U vs
601 Cervaiolo rainfall ($r = -0.64$, $df = 10$, $p < 0.05$) with a lag of 18 months. This complacency is to be
602 expected given the deep position of the cavern within the karst, and contrasts with many published
603 case studies (e.g. McDonald et al. 2004; Matthey et al. 2008; Treble et al. 2013; Tremaine & Froelich
604 2013), though not all (Matthey et al. 2010; McDonald et al. 2007), where overlying rock thickness is
605 sufficiently thin or permeable to record the effects of seasonal or event-based recharge variations on
606 trace element concentrations.

607



608

609 **Figure 7:** Scatterplots and Pearson r correlation coefficients of: (a) [Ba/Ca] vs [Sr/Ca]; (b) [Ba/Ca] vs [Mg/Ca]; and (c)
610 [Sr/Ca] vs [Mg/Ca] from Laghetto Basso pool waters. The underlined r value is statistically significant at $p < 0.05$.

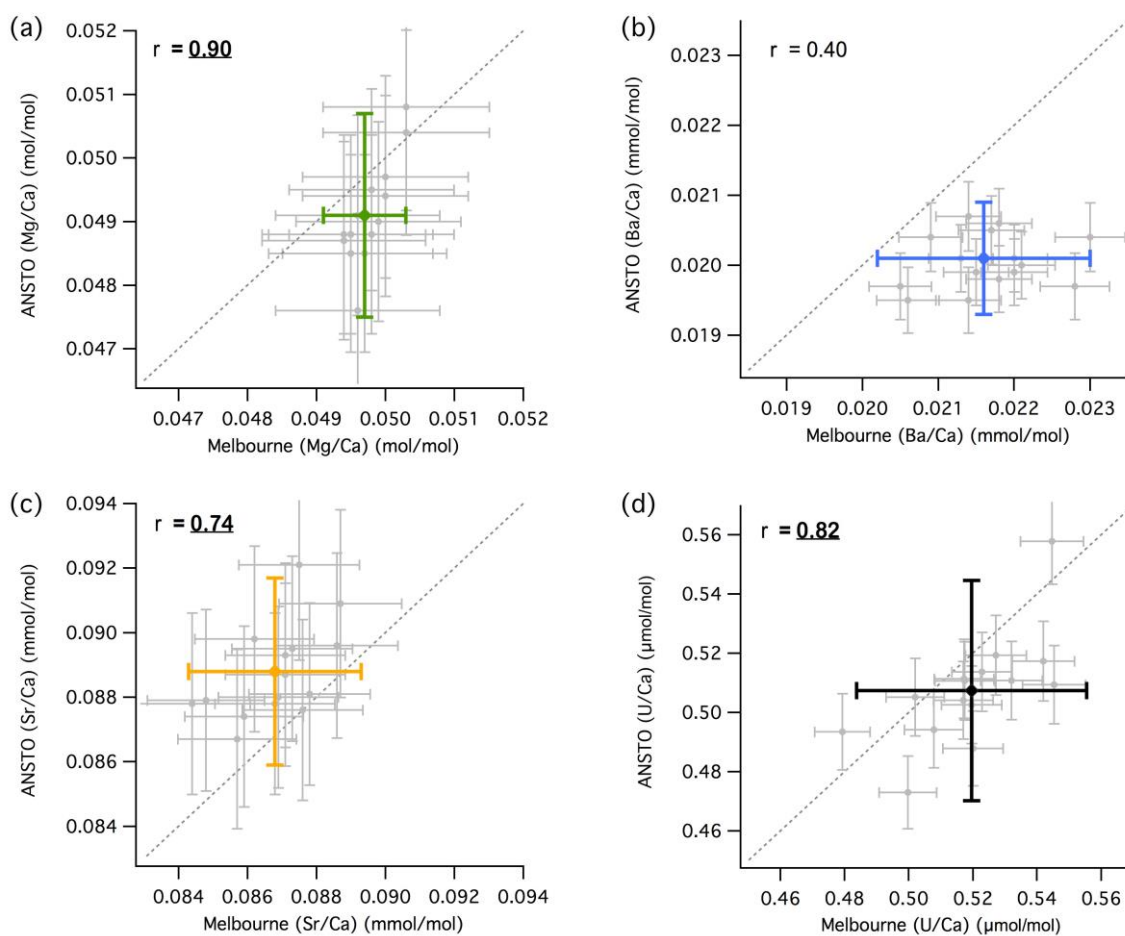
611

612 5.3 Trace element variations in ‘modern’ CD3 calcite

613 There is a degree of heterogeneous incorporation of trace elements into CD3-12 apparent from both
614 solution analysis of large (1 cm^2) surface scrapings and, in particular, the higher spatial-resolution
615 ($49 \mu\text{m}^2$) laser-spot analysis. Correlation coefficients for bivariate plots of the ANSTO and UM
616 solution-analysis results reveal statistically significant r values for [Mg/Ca], [Sr/Ca] and [U/Ca] (p
617 < 0.05 , two-tailed Pearson r correlation test) (**Fig. 8**). This indicates measurable inter-sample
618 differences in these ratios (see the row of per cent values in **Table 3**) even at such a coarse spatial
619 resolution, pointing to a degree of trace-element variability across the growing crystal surfaces.
620 Paired sets of solution results for [Ba/Ca], on the other hand, reveal no correlation (**Fig. 6**).

621

622 Both solution and laser datasets show consistent patterns in the degree of relative scatter around
 623 mean values, with Mg, Sr and Ba having the lowest scatter, and U having the highest scatter.
 624 However, the magnitude of scatter is greater – up to eight times for U – in the laser data. The
 625 detection and nature of such scatter is important because of the growing use of microanalytical
 626 techniques for measuring trace elements in speleothems (Fairchild & Baker 2012), which raises the
 627 issue of how representative of the average time-equivalent trace-element concentrations in
 628 speleothem calcite are the concentrations determined from one or even a few individual laser scan
 629 lines. This has implications for deriving meaningful quantitative or semi-quantitative
 630 palaeohydrological information from elemental ratios.
 631



632
 633 **Figure 8:** Scatterplots of individual Melbourne and ANSTO ICP-MS results for the CD3-12 calcite trace element ratios
 634 [Mg/Ca], 10^3 *[Sr/Ca], 10^3 *[Ba/Ca], and 10^6 *[U/Ca] (grey points), along with mean values (coloured points). All error
 635 bars are 2 s.d. uncertainties. The diagonal dashed line represents parity ($y = x$) between the two sets of analyses. Pearson
 636 r values are shown, with underlined values being statistically significant at $p \leq 0.05$ ($df = 13$, two-tailed test).
 637

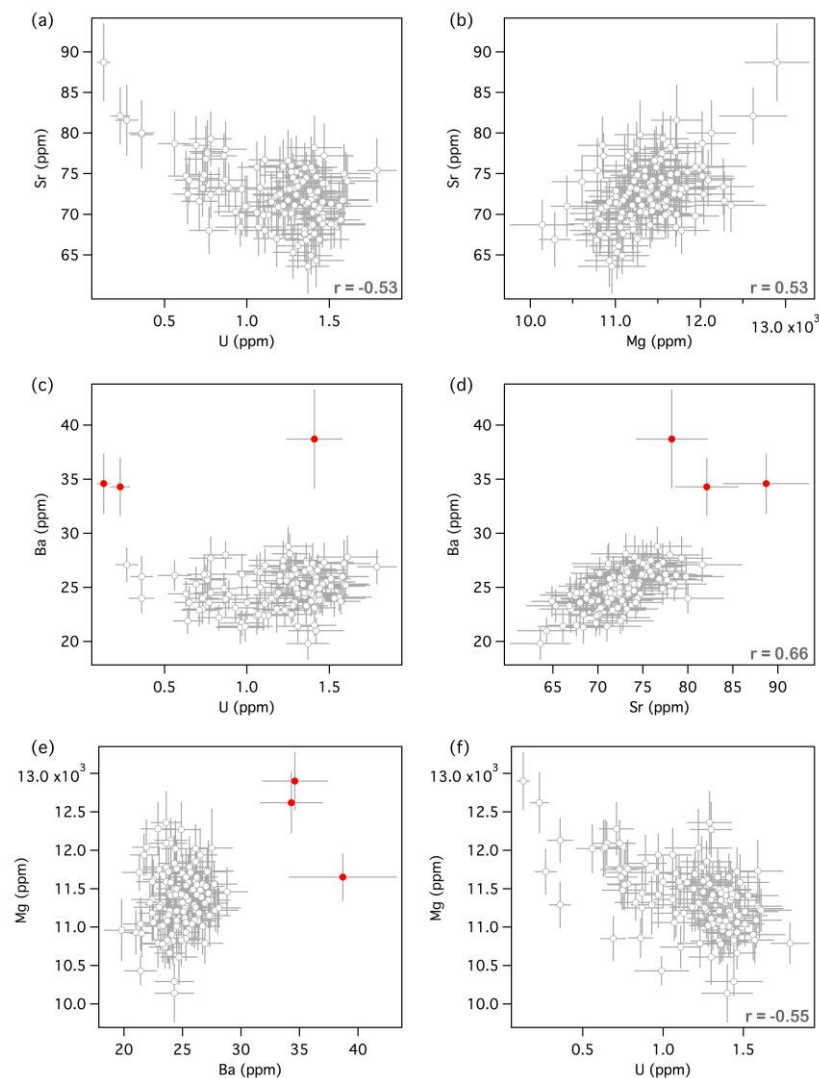
638 The notion of heterogenous incorporation of trace elements into time-equivalent regions of calcite is
 639 well-documented in both laboratory and natural settings (Fairchild & Baker 2012) and is referred to
 640 as compositional zoning. It can occur between different crystal sectors with non-equivalent faces
 641 (intersectoral zoning) (Reeder & Grams 1987; Reeder & Paquette 1990) or within the same crystal

642 sector (intra-sectoral zoning) (Paquette & Reeder 1995). In the case of the former, interfacial, time-
643 equivalent trace-element concentrations can vary by up to a factor of eight, and are attributed to
644 variable growth rates on different sectors or to the different surface structures characterising the
645 non-equivalent faces (Reeder & Paquette 1990). Intra-sectoral zoning occurs within a given single
646 sector and is caused by anisotropic layer growth, giving rise to step-selective affinities for foreign
647 ions that culminate in differential elemental partitioning (Paquette & Reeder 1990). As with
648 intersectoral zoning, it is related to the fundamental structural properties of the crystal surface, and
649 it co-exists with sectoral zoning (although the converse is not the case) (Paquette & Reeder 1995).

650

651 The traverse patterns evident in **Fig. 5** show some degree of covarying behaviour between pairs of
652 elements. Scatterplots and correlation coefficients using all of the laser spot data (**Fig. 9**) show
653 significant positive correlations between those elements regarded as being substituting ones (Ba vs
654 Sr, Sr vs Mg), whilst significant negative correlations occur between elements deemed to be
655 incompatible (U vs Mg, U vs Sr) (Reeder & Paquette 1990). This is consistent with the general
656 notion of compositional zoning (Paquette & Reeder 1990).

657



658

659 **Figure 9:** Scatterplots of all ($n = 120$) LA-ICP-MS calcite trace element spot data (Mg, Sr, Ba and U, all in ppm) shown
 660 in Figure 5. (a) Sr vs U; (b) Sr vs Mg; (c) Ba vs U; (d) Ba vs Sr; (e) Mg vs Ba; (f) Mg vs U. Error bars represent the
 661 measurement error from downhole ablation (2 s.e.). All Pearson r correlation coefficients shown are statistically
 662 significant at $p \leq 0.05$. Red symbols represent outlying Ba values excluded from all Ba vs X correlations.
 663

664 The tendency for U to have the greatest heterogeneity (in terms of proportional variability around
 665 the mean value) is consistent with patterns observed in a 2D image of this element produced from
 666 the Marine Isotope Stage (MIS) 7 and 8 section of another core drilled from CD3 (Figure 2d in
 667 Drysdale et al. 2012). In this image, dendritic zones of low U are visible, with the range of U
 668 concentrations (0.6 to 1.6 ppm) similar to that shown in **Fig. 5**; a hint of Sr and Ba zoning in the
 669 same regions of this image is also apparent. This pattern in U has since been shown to persist from
 670 the core top (modern) back to at least the MIS 12 section (our unpublished data), and whilst lying
 671 beyond the scope of this present work, a future multi-element study warrants further investigation.
 672 Such 2D patterns may be linked to the variations observed in **Fig. 5**, and is suggestive of either
 673 petrographic or crystallographic control of U (and potentially Sr and Ba) incorporation into calcite
 674 or selective leaching of U along specific crystal sectors.
 675

676 In oxidising environments, such as those of Laghetto Basso, U is usually present in its hexavalent
677 state U(VI) as the uranyl ion (UO_2^{2+}) (Langmuir 1978), which is capable of forming bonds with
678 ligands commonly found in natural waters (e.g. CO_3^{2-}) (Reeder et al. 2001). These are thought to be
679 incorporated into calcite through either coprecipitation or adsorption (e.g. via colloids). U
680 speciation is highly sensitive to pH (Langmuir 1978). Processing of the pool water hydrochemistry
681 data through the MINTEQ program reveals the presence of two dominant uranyl species: the
682 neutral complex $\text{Ca}_2\text{UO}_2(\text{CO}_3)_{3(\text{aq})}$ (~55-56%) and the anion $\text{CaUO}_2(\text{CO}_3)_2^{2-}$ (~41-42%). One
683 possible explanation for the wide range of U concentrations in time-equivalent calcite is the
684 incorporation of both of these species, each according to a different D_U . However, the affinity of the
685 neutral species for calcite is thought to be low because of the positive charge of a calcite surface at
686 the pH of Laghetto Basso waters (Chen et al. 2016). This implicates the uranyl anion as the form
687 most likely to be incorporated into CD3-12. Although adsorption onto colloidal phases might be
688 possible (Hartland et al. 2014; Wassenburg et al. 2016), the long travel path that percolation waters
689 take before reaching the GdS, and the low soil cover above the cave, would argue against a strong
690 presence of colloids in the pool waters. This points to the direct incorporation of uranyl into the
691 calcite, most likely by U^{6+} substitution for Ca^{2+} and two axial oxygen atoms substituting for the
692 carbonate ion (Kelly et al. 2003).

693

694 **5.4 Partition coefficients: comparison with previous studies**

695 *5.4.1 Introduction*

696 We now compare our calcite partition coefficients for Mg, Sr, Ba and U with previously published
697 values. Partition coefficients for calcite have been derived from a range of laboratory and natural
698 settings (Huang & Fairchild 2001; Tremaine & Froelich 2013), representing a diversity of physico-
699 chemical environments. For example, the strong interest in the study of trace elements in marine
700 carbonates has seen many laboratory studies where calcite has been farmed from solutions that
701 simulate seawater chemistry (Kitano & Oomori 1971; Mucci & Morse 1983; Burton & Walter 1991;
702 Yoshimura et al. 2015; Chen et al. 2016). Given the relatively narrow range of hydrogeochemical
703 conditions of most cave systems, the comparisons we make below are largely restricted to
704 coefficients derived from field studies of caves (Holland et al. 1964; Gascoyne 1983; Huang et al.
705 2001; Karmann et al. 2007; Fairchild et al. 2010; Tremaine & Froelich 2013) and cave-analogue
706 laboratory studies (Huang & Fairchild 2001; Day & Henderson 2013) (**Table 5**).

707

708 An unavoidable problem of deriving calcite partition coefficients in cave studies is the stability of
709 the solution [X/Ca] values at each monitoring station within the cave through the period of each
710 calcite harvest. Source-water [X/Ca] values can change relatively rapidly (e.g. McDonald et al.

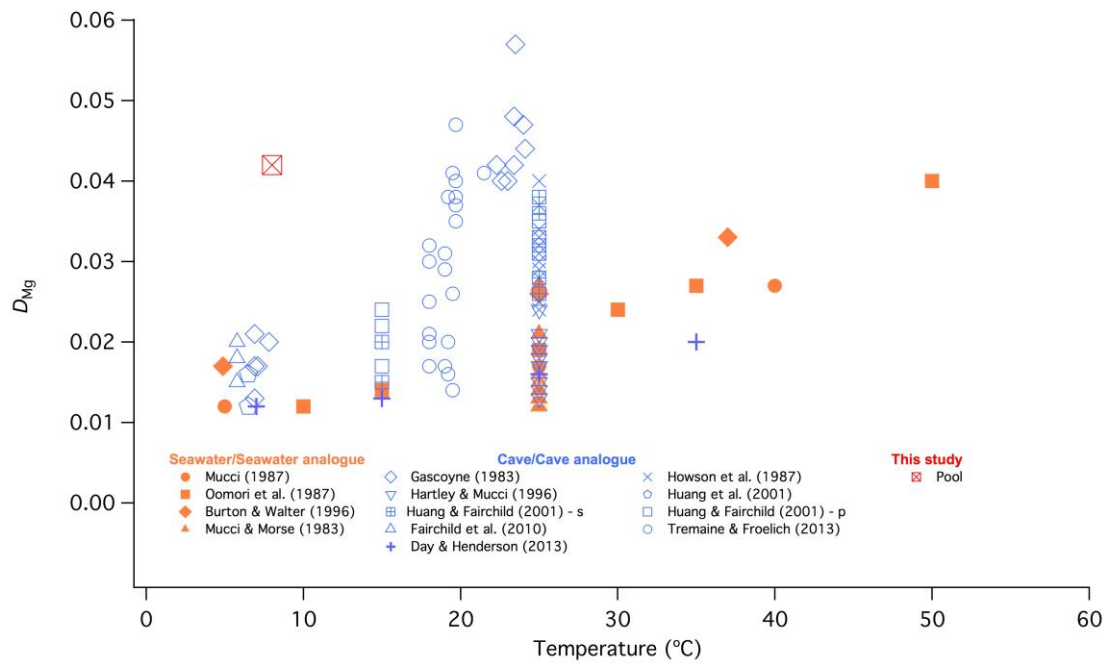
711 2004; Tremaine & Froelich 2013), and although it is common to average before and after (or more)
712 values over the period of calcite growth, it is not possible to determine the weighting of each
713 individual [X/Ca] value without some form of continuous monitoring, or at least very intensive (e.g.
714 monthly) sampling. An additional potential problem in cave studies is whether or not farmed calcite
715 (e.g. by precipitation onto glass plates) is truly representative of natural calcite growth, particularly
716 in the context of crystal growth and morphology effects on element partitioning. This is also an
717 issue for cave-analogue studies, which, like other related laboratory (e.g. seawater-analogue)
718 experiments, suffer the additional problem of using synthetically prepared solutions. In this study,
719 we have attempted to overcome these issues by targeting a very deep cave environment
720 characterised by relatively stable hydrochemistry, and by sampling naturally grown calcite.

721

722 5.4.2 Magnesium

723 The D_{Mg} for Laghetto Basso (0.042 ± 0.002) is one the highest mean values ever recorded for cave
724 or cave-analogue conditions, being exceeded in mean values only by Gascoyne (1983) in his study
725 of Jamaican cave calcite (**Table 5**). Considering the thermodynamic tendency for D_{Mg} to vary
726 positively with temperature (Katz 1973; Gascoyne 1983; Mucci & Morse 1983; Burton & Walter
727 1991; Huang & Fairchild 2001; Day & Henderson 2013), the high value is surprising given the
728 relatively low temperatures of Laghetto Basso waters (~ 8 °C) and the expectation that during
729 warmer periods (all other things being equal) the pool waters would produce even higher D_{Mg}
730 values. Potential reasons for such a high D_{Mg} at this low temperature include the pool water
731 [Mg/Ca], which is high for karst waters (~ 1.2). To examine this possibility further, we compared
732 the Laghetto Basso D_{Mg} with data from a range of seawater or seawater-analogue studies, where the
733 solution [Mg/Ca] reaches up to 20. As **Fig. 10** shows, the slopes of temperature vs D_{Mg} from these
734 studies (Mucci 1987; Oomori et al. 1987; Burton and Walter 1991) fall within the scatter of
735 temperature vs D_{Mg} for cave and cave-analogue studies, where [Mg/Ca] is <1 , suggesting that
736 [Mg/Ca] is not significant. Mucci & Morse (1983), however, report an increase in D_{Mg} from 0.012
737 to 0.027 at 25°C as the solution [Mg/Ca] decreases from 7.5 to 1, but an identical experiment
738 conducted at Laghetto Basso temperatures using a solution [Mg/Ca] ≈ 1 would produce significantly
739 *lower* D_{Mg} values given the temperature/ D_{Mg} relationship. Therefore, we disqualify the high pool-
740 water [Mg/Ca] as the reason for the unusually high Laghetto Basso D_{Mg} .

741



742

743 **Figure 10:** Comparison of D_{Mg} values versus temperature between a range of published cave/cave analogue (blue
 744 symbols) and seawater-analogue studies (orange symbols) and this study (red symbols). The straw (s) and plate (p)
 745 values are shown separately for the Huang & Fairchild (2001) data.

746

747 Source-water PCO_2 and saturation state, the reaction rate and crystal nucleation style have also been
 748 considered as possible drivers of D_{Mg} variations (Howson et al. 1987; Huang & Fairchild 2001;
 749 Hartley & Mucci 1996; Mavromatis et al. 2013), but these have been either rejected as having
 750 negligible influence (PCO_2) or their effects can be ruled out in the case of Laghetto Basso because
 751 the direction of D_{Mg} change is contrary to what would be expected. For example, homogeneous
 752 nucleation is thought to drive D_{Mg} values lower, but many experimental studies include crystal
 753 seeding (e.g. Huang & Fairchild 2001; Day & Henderson 2013) to mimic the heterogeneous
 754 nucleation observed in marine and cave settings. The results of cave-analogue experiments
 755 conducted in this way still yield D_{Mg} values much lower than Laghetto Basso at or near the
 756 observed pool temperatures. The effects of growth rate and saturation state were investigated
 757 recently by Mavromatis et al. (2013) at 25°C and 1 atm PCO_2 , who found clear increases in D_{Mg}
 758 with both variables. However, these factors cannot explain the high D_{Mg} in Laghetto Basso calcite,
 759 given that the relatively low saturation state of the waters, and the very low growth rates, plus
 760 cooler temperatures, would yield even higher D_{Mg} at the experimental conditions used by
 761 Mavromatis et al. (2013). In a study of a Florida cave, Tremaine and Froelich (2013) produced a
 762 detailed dataset of paired growth rates and D_{Mg} (and D_{Sr}) within a narrow range of cave
 763 temperatures (18 – 21.5°C), but despite a considerable range in coefficients, no relationship is
 764 observed.

765

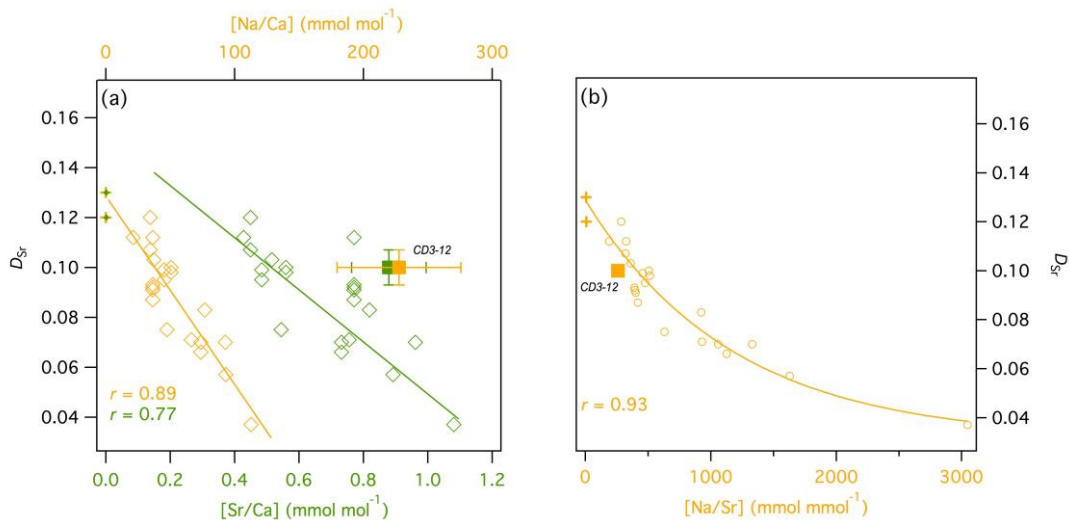
766 The unusually high D_{Mg} value for Laghetto Basso calcite possibly owes its origin to the low-ionic
767 strength and low-saturation-state of its source waters, which, in addition to the hydrodynamics of a
768 subaqueous setting, give rise to the excessively slow growth rates of CD3. Such unusual conditions
769 for a speleothem have not been encountered in previous cave and cave-analogue investigations.
770 Recently, a comparison of modern calcite and pool waters from Laghetto Basso and Devils Hole
771 (Nevada, USA) (Daëron et al. 2019) has suggested that the depositional conditions at these two sites
772 are likely to approximate thermodynamic isotopic equilibrium, or at least closer to equilibrium
773 compared to previous studies. Combining isotopic information from both sites across a temperature
774 range spanning most speleothem settings (~8 and 34 °C) produces calcite clumped-isotope
775 calibration and conventional oxygen isotope fractionation curves that are significantly offset from
776 those of calcites formed under different depositional conditions. Like Laghetto Basso, Devils Hole
777 calcite growth rates are extremely slow on account of the hydrochemistry and hydrodynamic setting
778 (Plummer et al. 2000). It would be useful to conduct future cave-analogue studies that mimic
779 subaqueous environments like Laghetto Basso to examine D_{Mg} and other D_X across a range of
780 growth rate, temperature and low-ionic-strength conditions.

781

782 5.4.3 Strontium

783 The mean D_{Sr} for Laghetto Basso (0.100 ± 0.007 ; **Table 4**) lies within the range of values observed
784 in other cave studies. As with Mg, the partitioning of Sr into calcite has been the subject of
785 considerable study in both natural and laboratory cave settings as well as marine applications
786 (Böttcher & Dietzel 2010). The numerous possible factors driving D_{Sr} variations in marine studies
787 have also been explored for speleothems, notably temperature, solution [Sr/Ca], [Mg/Ca] and
788 [Na/Ca], and growth rate. In two detailed cave-analogue studies and one natural cave study,
789 Fairchild & Huang (2001), Day & Henderson (2013) and Tremaine & Froelich (2013) each found
790 no relationship between D_{Sr} and either growth rate or temperature. Huang & Fairchild (2001),
791 however, concluded that the low Na concentrations used in their experimental solutions may have
792 contributed to their D_{Sr} being higher than those from seawater-analogue studies, where much higher
793 Na concentrations are used. This is because the Na ion is thought to outcompete Sr for non-lattice
794 sites on the calcite crystal (Pingitore & Eastman 1986). Although there has been no subsequent
795 systematic study since Huang and Fairchild (2001) on the effects of solution [Na/Ca], [Sr/Ca] and
796 [Mg/Ca] on D_{Sr} in cave or cave-analogue settings, the data presented in Tremaine & Froelich (2013)
797 (their Supplementary Table EC.1) contain a sufficient spread of both solution [X/Ca] and D_{Sr} values
798 to test this. Statistically significant negative correlations are found for [Na/Ca] versus D_{Sr} ($r = -0.89$)
799 and [Sr/Ca] versus D_{Sr} ($r = -0.77$) (**Fig. 11a**); no significant correlation exists for [Mg/Ca] versus
800 D_{Sr} . Although we do not have individual calcite-water [X/Ca] pairs to perform precisely the same

801 test on the pool-water/CD3-12 data, we can see that the [Sr/Ca] versus D_{Sr} for CD3-12 (closed
 802 green diamonds, **Fig. 11a**) lies close to the scatter in the Tremaine & Froelich (2013) data. Further,
 803 the [Na/Ca] versus D_{Sr} for CD3-12 lie well clear of the corresponding Tremaine & Froelich (2013)
 804 values. Given the proposed effects of Na described above (Pingitore & Eastman 1986), the
 805 relatively high Na concentrations in Laghetto Basso should yield lower D_{Sr} if Na concentrations *per*
 806 *se* were important. A more robust test of the effects of Na is to use [Na/Sr] instead of [Na/Ca]: if Na
 807 outcompetes Sr for lattice sites then this should be evident in the ratio of these two elements. As
 808 shown in **Fig. 11b**, this is indeed the case: a significant negative exponential relationship exists
 809 between [Na/Sr] and D_{Sr} based on the data from Tremaine and Froelich (2013), and Day and
 810 Henderson (2013).



811
 812
 813 **Figure 11:** (a) Scatterplots of [Na/Ca] vs D_{Sr} (orange symbols) and [Sr/Ca] versus D_{Sr} (green symbols) for data
 814 presented in Tremaine and Froelich (2013) (open diamonds), Day and Henderson (2013) (crosses) and this study (CD3-
 815 12: solid squares). The Pearson r correlation coefficients are statistically significant ($df = 19, p < 0.05$) and correspond
 816 to the Tremaine and Froelich (2013) data only. (b) Scatterplot of [Na/Sr] vs D_{Sr} for the same studies shown in (a). The
 817 exponential fit, which models all data shown, is described by the equation $y = 0.1173e^{-0.0004x}$ and is statistically
 818 significant ($df = 24, p < 0.05$).
 819

820
 821 **5.4.3 Barium and Uranium**

822 The partitioning of Ba and U into calcite has not been the explicit subject of experimental cave
 823 investigations. The only cave-analogue study is that of Day and Henderson (2013), who reported a
 824 mean D_{Ba} value slightly larger than that for CD3-12. Although the study of Day and Henderson
 825 (2013) was conducted at temperatures (25° and 35°C) that are significantly higher than that of the
 826 Laghetto Basso water, temperature is not regarded as important in controlling D_{Ba} (Lea & Spero
 827 1994). Growth rate and solution [Ba/Ca] have been linked to variations in D_{Ba} (Pingitore &
 828 Eastman 1984; Tesoriero & Pankow 1996), with higher growth rates producing higher D_{Ba} .
 829 However, these relationships have only been observed once growth rates and [Ba/Ca] greatly

830 exceed those of CD3-12. Day and Henderson (2013) observed no relationship between growth rate
831 and D_{Ba} (or D_U).

832

833 Uranium partitioning has been shown to vary with growth rate and temperature. The D_U values for
834 CD3-12 (0.013 ± 0.002) are between 5 and 9 times below those experimentally determined by Day
835 and Henderson (2013) (**Table 4**). They found a weak negative relationship between temperature
836 and D_U , with values decreasing from 0.11 ± 0.011 to 0.062 ± 0.012 as temperature rose from 7°C to
837 35°C. However, the value for CD3-12 is almost an order of magnitude lower than Day and
838 Henderson (2013) at similar temperatures.

839

840 Several studies have evaluated the effects of growth rate on D_U . Weremeichik et al. (2017)
841 determined that D_U increased from 0.02 to 0.06 as growth rate increased from 0.01 to 0.14 nm s⁻¹.
842 Although the Holocene growth rates observed in CD3-12 (1.24×10^{-5} nm s⁻¹) are several orders of
843 magnitude lower than these, the direction of D_U change is consistent. Further, the starting solution
844 [U/Ca] used by Weremeichik et al. (2017) (0.919 mmol/mol) is ~24 times higher than the Corchia
845 pool water [U/Ca]. The much slower growth rates in the pool implies that the calcite crystals remain
846 exposed to the solution for much longer before being ‘protected’ by further calcite growth. This
847 would facilitate leaching or desorption of uranyl carbonate from the calcite lattice, given the high
848 solubility of this species.

849

850 **6. CONCLUSIONS**

851 In this study, we have sought to advance understanding of how trace elements are incorporated into
852 natural calcites by investigating the partitioning of Mg, Sr, Ba and U into subaqueous cave calcite, a
853 rarely studied form of speleothem. We have shown that the pool-water chemistry of Laghetto Basso
854 displays decadal-scale stability, in contrast to percolation-waters reported in a number of other cave
855 studies (e.g. Fairchild et al. 2000; McDonald et al. 2004; Tremaine & Froelich 2013). This produces
856 relatively well-constrained solution [X/Ca] from which to derive D_X values. We have measured
857 [X/Ca] on ‘modern’ subaqueous calcite (CD3-12) that grows naturally from these pool waters,
858 rather than calcite grown on seeded, artificial substrata or from synthetic solutions under laboratory
859 conditions.

860

861 Several lines of evidence indicate that the outer surface of CD3 is actively depositing today. These
862 include a U-Th chronology corrected to an independently dated age profile of a stalagmite from the
863 same cave chamber, the supersaturated state of the pool water, and the fact that the speleothem has
864 grown over multiple glacial-interglacial cycles (Drysdale et al. 2012). The slow growth rates of

865 CD3-12, the challenge of sampling its active outer growth surface, and the potential for time-
866 equivalent layers of non-uniform thickness prevent us from unequivocally determining that the
867 calcite grew exclusively across the monitoring period. However, the stability of the pool-water
868 chemistry over a 15-year period (1997 to 2012) suggests at least decadal-scale hydrochemical
869 stability, conducive to precipitating relatively invariant calcite [X/Ca]. This is validated by the
870 statistically indistinguishable mean CD3-12 [X/Ca] values from the surface (analysed by solution
871 ICP-MS and incorporating, no more than ~300 years of growth) and the outermost 7 μm of calcite
872 (analysed by LA-ICP-MS and incorporating ~21 years of growth). Taking these solution and calcite
873 results together, we have circumvented the issue of having to average (often quite different)
874 instantaneous solution [X/Ca] values for pairing with the [X/Ca] from calcite grown over the same
875 period. We argue that the mean D_X values from CD3-12 therefore represent reliable estimates of
876 partition coefficients from naturally grown subaqueous calcite.

877

878 Comparison with published studies reveals that the mean D_{Mg} value from CD3-12 is significantly
879 higher than values produced from other cave and cave-analogue (and indeed, sea-water analogue)
880 situations given the low pool-water temperature. This may be facilitated by the extremely slow
881 growth rates of the speleothem. Future calcite/source-water studies conducted in broadly similar
882 cave-pool settings but at sites with different temperatures, could enable quantification of D_{Mg} -
883 temperature relationships. However, we suspect that finding appropriate sites (dolomitic bedrock,
884 low-ionic strength waters, deep-set cavern) would prove rather challenging, and laboratory
885 simulations might be the most appropriate approach in this regard.

886

887 The D_{Sr} values for CD3-12 are comparable with published cave/cave analogue studies, the few data
888 available suggest that [Na/Sr] might be an important factor in controlling Sr partitioning through Na
889 outcompeting Sr for compatible non-lattice sites. The long exposure time of the CD3-12 calcite
890 surface, where growth rates are a mere ~0.3 – 0.4 μm per year (averaged over the Holocene), raises
891 the prospect of dissolution of soluble uranyl carbonate. This could explain the higher variability of
892 U partitioning and low mean D_{U} shown here, as well as the dendritic zones of low U concentration
893 observed throughout the upper half of CD3-12, including the MIS 8-7 section reported in Drysdale
894 et al. (2012).

895

896 In spite of the relatively well-constrained D_X values obtained, data from both the surface calcite and
897 the outermost 7 μm reveal heterogeneity in trace element distribution in CD3-12, which, as
898 expected, is more evident in the better-resolved laser data. A number of the laser profiles show
899 covariation amongst elements, suggesting that element incorporation may be influenced by

900 compositional zoning or fabric effects. Mapping the spatial patterns of elemental variation in 2D is
901 necessary to determine the presence / extent of compositional zoning. It would enable the
902 quantification of the range of elemental concentrations, and reveal if zoning bears any relationship
903 to the prevailing climate state, upon which speleothem growth rates and hydrochemistry depend.

904

905 Single subaqueous speleothems can preserve continuous palaeoclimate records spanning many
906 hundreds of thousands of years (Winograd et al. 1992). The subaqueous speleothem used in the
907 present study captures a palaeoclimate record spanning almost the last one million years (Drysdale
908 et al. 2012). As demonstrated by previous research on stalagmites and flowstones (Drysdale et al.
909 2006; Johnson et al. 2006; Wong et al. 2011; Hartmann et al. 2013; Weber et al. 2018), trace-
910 element changes have the potential to complement stable-isotope records from this speleothem, and
911 to play a key role in developing robust interpretations of regional palaeoclimate and wider
912 environmental changes (e.g. long-term landscape evolution) over multiple glacial-interglacial cycles.
913 The current study has laid the foundations for additional extensive trace element study of CD3 by
914 deriving partitioning coefficients under modern conditions. Future work will focus on long-term
915 trace element changes and the palaeoclimate drivers, particularly whether elements considered to be
916 useful hydrological tracers from previous speleothem studies also preserve palaeohydrological
917 information in CD3. However, given the slow growth rates and relatively complacent decadal-scale
918 hydrochemistry, palaeohydrological changes would likely only be resolved at centennial or greater
919 (e.g. millennial or orbital) time scales.

920

921

922

923 **ACKNOWLEDGEMENTS**

924 This research was supported by funding from the Australian Research Council (Discovery Project
925 number DP160102969, awarded to RD, GZ, ER and JW; Laureate Fellowship FL160100028
926 awarded to JW; and Future Fellowship FT130100801 awarded to JH. We are grateful to the Gruppo
927 Speleologico Lucchese and the Federazione Speleologica Toscana for outstanding support. This
928 paper benefitted from discussions with Professor Richard Reeder. This paper has benefitted
929 significantly from three very meticulous and constructive reviews, for which we are very grateful.

930

931

932

933 **REFERENCES**

- 934 Azzaro, E., Negretti, G. and Tucci, P. (1987) A chemiostratigraphic study of the metadolomitic
935 sequence of the southern side of Mount Corchia (Alpi Apuane, Italy). *Geologica Rom.* 26,
936 293-303.
- 937 Bajo, P., Drysdale, R.N., Woodhead, J.D., Hellstrom, J.C., Zanchetta, G. 2012. High-resolution U-
938 Pb dating of an Early Pleistocene stalagmite from Corchia Cave (central Italy). *Quatern.*
939 *Geochronology* 14, 5-17.
- 940 Bajo, P., Borsato, A., Drysdale, R., Hua, Q., Frisia, S., Zanchetta, G., Hellstrom, J. and Woodhead,
941 J. (2017) Stalagmite carbon isotopes and dead carbon proportion (DCP) in a near-closed-
942 system situation: An interplay between sulphuric and carbonic acid dissolution. *Geochim.*
943 *Cosmochim. Acta* 210, 208-227.
- 944 Bajo, P., Hellstrom, J., Frisia, S., Drysdale, R., Black, J., Woodhead, J., Borsato, A., Zanchetta, G.,
945 Wallace, M.W., Regattieri, E. and Haese, R. (2016) “Cryptic” diagenesis and its implications
946 for speleothem geochronologies. *Quatern. Sci. Rev.* 148, 17-28.
- 947 Balboni, E., Morrison, J.M., Wang, Z., Engelhard, M.H. and Burns, P.C. (2015) Incorporation of
948 Np(V) and U(VI) in carbonate and sulfate minerals crystallized from aqueous solution.
949 *Geochim. Cosmochim. Acta* 151, 133-149.
- 950 Baneschi, I., Piccini, L., Regattieri, E., Isola, I., Guidi, M., Lotti, L., Mantelli, F., Menichetti, M.,
951 Drysdale, R.N. and Zanchetta, G. (2011) Hypogean microclimatology and hydrology of the
952 800-900 m asl level in the Monte Corchia cave (Tuscany, Italy): preliminary considerations
953 and implications for paleoclimatological studies. *Acta Carsologica* 40, 175-187.
- 954 Bernal, J.P., Cruz, F.W., Strikis, N.M., Wang, X., Deininger, M., Catunda, M.C.A., Ortega-
955 Obregón, C., Cheng, H., Edwards, R.L. and Auler, A.S. (2016) High-resolution Holocene
956 South American monsoon history recorded by a speleothem from Botuverá Cave, Brazil.
957 *Earth and Planetary Science Letters* 450, 186-196.
- 958 Borsato, A., Frisia, S., Fairchild, I.J., Somogyi, A. and Susini, J. (2007) Trace element distribution
959 in annual stalagmite laminae mapped by micrometer-resolution X-ray fluorescence:
960 Implications for incorporation of environmentally significant species. *Geochim. Cosmochim.*
961 *Acta* 71, 1494-1512.
- 962 Böttcher, M.E. and Dietzel, M. (2010) Metal-ion partitioning during low-temperature precipitation
963 and dissolution of anhydrous carbonates and sulphates. *EMU Notes in Mineralogy* 10, 139-
964 187.
- 965 Bourdin, C., Douville, E. and Genty, D. (2011) Alkaline-earth metal and rare-earth element
966 incorporation control by ionic radius and growth rate on a stalagmite from the Chauvet Cave,
967 Southeastern France. *Chem. Geol.* 290, 1-11.

- 968 Burton, E.A. and Walter, L.M. (1991) The effects of P_{CO_2} and temperature on magnesium
969 incorporation in calcite in seawater and $MgCl_2$ - $CaCl_2$ solutions. *Geochim. Cosmochim. Acta*
970 55, 777-785.
- 971 Busenberg, E. and Niel Plummer, L. (1989) Thermodynamics of magnesian calcite solid-solutions
972 at 25°C and 1 atm total pressure. *Geochim. Cosmochim. Acta* 53, 1189-1208.
- 973 Busenberg, E. and Plummer, N. (1982) The kinetics of dissolution of dolomite in CO_2 - H_2O systems
974 at 1.5 to 65°C and 0 to 1 atm PCO_2 . *Amer. J. Sci.* 282, 45-78.
- 975 Carmignani, L. and Giglia, G. (1984) "Autoctono Apuano" e Falda Toscana. Sintesi dei dati e delle
976 interpretazionini, Cento anni di Geologia Italiana. Pitagora, Bologna, pp. 199-214.
- 977 Carmignani, L. and Kligfield, R. (1990) Crustal extension in the northern Apennines: The transition
978 from compression to extension in the Alpi Apuane Core Complex. *Tectonics* 9, 1275-1303.
- 979 Casteel, R.C. and Banner, J.L. (2015) Temperature-driven seasonal calcite growth and drip water
980 trace element variations in a well-ventilated Texas cave: Implications for speleothem
981 paleoclimate studies. *Chem. Geol.* 392, 43-58.
- 982 Chen, X., Romaniello, S.J., Herrmann, A.D., Wasylenki, L.E., Anbar, A.D. (2016) Uranium isotope
983 fractionation during coprecipitation with aragonite and calcite. *Geochim. Cosmochim. Acta*
984 188, 189-207.
- 985 Cheng, H., Edwards, R.L., Broecker, W.S., Denton, G.H., Kong, X., Wang, Y., Zhang, R. and
986 Wang, X. (2009) Ice age terminations. *Science* 326, 248-252.
- 987 Cheng, H., Edwards, R.L., Sinha, A., Spötl, C., Yi, L., Chen, S., Kelly, M., Kathayat, G., Wang, X.,
988 Li, X., Kong, X., Wang, Y., Ning, Y. and Zhang, H. (2016) The Asian monsoon over the past
989 640,000 years and ice age terminations. *Nature* 534, 640-648.
- 990 Conti, P., Di Pisa, A., Gattiglio, M. and Meccheri, M. (1993) The Pre-Alpine Basement in the Alpi
991 Apuane (Northern Apennines, Italy), in: von Raumer, J.F., Neubauer, F. (Eds.), *Pre-Mesozoic*
992 *Geology in the Alps*. Springer Berlin Heidelberg, Berlin, Heidelberg, pp. 609-621.
- 993 Cortecchi, G., Dinelli, E., Indrizzi, M.C., Susini, C. and Adorni Braccesi, A. (1999) The Apuane
994 Alps metamorphic complex, Northern Tuscany: chemical and isotopic features of Grezzoni
995 and Marmi dolomitici. *Atti Soc. Tosc. Sci. Nat., Mem., Serie A* 106, 79-89.
- 996 Cruz, F.W., Burns, S.J., Jercinovic, M., Karmann, I., Sharp, W.D. and Vuille, M. (2007) Evidence
997 of rainfall variations in Southern Brazil from trace element ratios (Mg/Ca and Sr/Ca) in a Late
998 Pleistocene stalagmite. *Geochim. Cosmochim. Acta* 71, 2250-2263.
- 999 Daeron, M., Drysdale, R., Peral, M., Huyghe, D., Blamart, D., Coplen, T., Lartud, F. & Zanchetta,
1000 G. (2019) Most Earth-surface calcites precipitated out of isotopic equilibrium. *Nature*
1001 *Communications* doi.org/10.1038/s41467-019-08336-5.

- 1002 Day, C.C. and Henderson, G.M. (2013) Controls on trace-element partitioning in cave-analogue
1003 calcite. *Geochim. Cosmochim. Acta* 120, 612-627.
- 1004 Drysdale, R.N. (2001) Factors controlling the hydrochemistry of Louie Creek, a
1005 travertinedepositing stream in the seasonally wet tropics of northern Australia. *Mar.*
1006 *Freshwater Res.* 52, 793-804.
- 1007 Drysdale, R., Zanchetta, G., Hellstrom, J.C., Zhao, J-x, Fallick, A.C., Isola, I., Bruschi, G. (2004)
1008 Palaeoclimatic implications of the growth history and stable isotope ($\delta^{18}\text{O}$ and $\delta^{13}\text{C}$)
1009 geochemistry of a Middle to Late Pleistocene stalagmite from central-western Italy. *Earth and*
1010 *Planetary Science Letters* 227, 215-229.
- 1011 Drysdale, R.N., Zanchetta, G., Hellstrom, J.C., Fallick, A.E. and Zhao, J.X. (2005) Stalagmite
1012 evidence for the onset of the Last Interglacial in southern Europe at 129 ± 1 ka. *Geophys. Res.*
1013 *Lett.* 32, L24708, doi:24710.21029/22005GL024658.
- 1014 Drysdale, R.N., Zanchetta, G., Hellstrom, J., Maas, R., Fallick, A., Pickett, M., Cartwright, I. and
1015 Piccini, L. (2006) Late Holocene drought responsible for the collapse of Old World
1016 civilizations is recorded in an Italian cave flowstone. *Geology* 34, 101-104.
- 1017 Drysdale, R., Hellstrom, J., Couchoud, I., Zanchetta, G., Woodhead, J., Greig, A., Fallick, A., Isola,
1018 I. (2008) Towards a new radiometrically dated North Atlantic palaeo-climate record covering
1019 the last million years: preliminary results from Corchia Cave speleothems, Italy. European
1020 Geosciences Union abstract EGU2008-A-05940.
- 1021 Drysdale R. N., Paul B. T., Hellstrom J. C., Couchoud I., Greig A., Bajo P., Zanchetta G., Isola I.,
1022 Spötl C., Baneschi I., Regattieri, E. and Woodhead J. D. (2012) Precise microsampling of
1023 poorly laminated speleothems for U-series dating. *Quat. Geochronol.* 14, 38–47.
- 1024 Edwards, R.L., Gallup, C.D., Ludwig, K.R., Simmons, K.R., Winograd, I.J., Szabo, B.J. and Riggs,
1025 A.C. (1993) Dating of the Devils Hole calcite vein. *Science* 259, 1626-1627.
- 1026 Fairchild, I.J. and Baker, A. (2012) *Speleothem science: From process to past environments*. Wiley-
1027 Blackwell.
- 1028 Fairchild, I.J., Baker, A., Borsato, A., Frisia, S., Hinton, R.W., McDermott, F. and Tooth, A.F.
1029 (2001) Annual to sub-annual resolution of multiple trace-element trends in speleothems. *J.*
1030 *Geol. Soc.* 158, 831-841.
- 1031 Fairchild, I.J., Borsato, A., Tooth, A.F., Frisia, S., Hawkesworth, C.J., Huang, Y., McDermott, F.
1032 and Spiro, B. (2000) Controls on trace element (Sr-Mg) compositions of carbonate cave
1033 waters: implications for speleothem climatic records. *Chem. Geol.* 166, 255-269.
- 1034 Fairchild, I.J., Spötl, C., Frisia, S., Borsato, A., Susini, J., Wynn, P.M. and Causid, J. (2010)
1035 Petrology and geochemistry of annually laminated stalagmites from an Alpine cave (Obir,
1036 Austria): seasonal cave physiology. *Geol. Soc. London, Spec. Pub.* 336, 295-321.

- 1037 Fairchild, I.J. and Treble, P.C. (2009) Trace elements in speleothems as recorders of environmental
1038 change. *Quatern. Sci. Rev.* 28, 449-468.
- 1039 Fohlmeister, J., Schröder-Ritzrau, A., Scholz, D., Spötl, C., Riechelmann, D.F.C., Mudelsee, M.,
1040 Wackerbarth, A., Gerdes, A., Riechelmann, S., Immenhauser, A., Richter, D.K. and Mangini,
1041 A. (2012) Bunker Cave stalagmites: An archive for central European Holocene climate
1042 variability. *Climate of the Past* 8, 1751-1764.
- 1043 Frisia, S. (2015) Microstratigraphic logging of calcite fabrics in speleothems as tool for
1044 palaeoclimate studies. *Int. J. Speleol.* 44, 1-16.
- 1045 Gascoyne, M. (1983) Trace element partition coefficients in the calcite-water system and their
1046 paleoclimatic significance in cave studies. *J. Hydrol* 61, 213-222.
- 1047 Gran, G. (1952) Determination of the equivalence point in potentiometric titrations. Part II. *Analyst*
1048 77, 661-671.
- 1049 Genty, D. & Massault, M. (1999) Carbon transfer dynamics from bomb ^{14}C and d^{13}C times series
1050 of a laminated stalagmite from SW France: modelling and comparison with other stalagmites.
1051 *Geochimica et Cosmochimica Acta* 63, 1537–1548.
- 1052 Griffiths, M., Drysdale, R., Gagan, M., Zhao, J-x., Ayliffe, L., Hantoro, W., Frisia, S., Hellstrom, J.,
1053 Fischer, M. Feng, J-x., Suwargadi, B. (2010). Multi-proxy stalagmite evidence for east
1054 Indonesian monsoon variability during the Holocene. *Earth and Planetary Science Letters*
1055 292, 27-38.
- 1056 Griffiths, M.L., Fohlmeister, J., Drysdale, R.N., Hua, Q., Johnson, K.R., Hellstrom, J.C., Gagan,
1057 M.K., Zhao, J-x. 2012. Hydrological control on the dead-carbon content of a Holocene
1058 tropical speleothem. *Quatern. Geochronology* doi:10.1016/j.quageo.2012.04. 001.
- 1059 Hartland, A., Fairchild, I.J., Müller, W. and Dominguez-Villar, D. (2014) Preservation of NOM-
1060 metal complexes in a modern hyperalkaline stalagmite: Implications for speleothem trace
1061 element geochemistry. *Geochim. Cosmochim. Acta* 128, 29-43.
- 1062 Hartley, G. and Mucci, A. (1996) The influence of P_{CO_2} on the partitioning of magnesium in calcite
1063 overgrowths precipitated from artificial seawater at 25° and 1 atm total pressure. *Geochim.*
1064 *Cosmochim. Acta* 60, 315-324.
- 1065 Hartmann, A., Eiche, E., Neumann, T., Fohlmeister, J., Schröder-Ritzrau, A., Mangini, A. and
1066 Haryono, E. (2013) Multi-proxy evidence for human-induced deforestation and cultivation
1067 from a late Holocene stalagmite from middle java, Indonesia. *Chemical Geology* 357, 8-17.
- 1068 Hellstrom, J. and McCulloch, M. (2000) Multi-proxy constraints on the climatic significance of
1069 trace element records from a New-Zealand speleothem. *Earth Planet. Sci. Lett.* 179, 287-297.

- 1070 Hellstrom, J., Paton, C., Woodhead, J. and Hergt, J. (2008) Iolite: software for spatially resolved
1071 LA-(quad and MC) ICPMS analysis, in: Sylvester, P. (Ed.), *Laser Ablation ICP-MS in the*
1072 *Earth Sciences: Current Practices and Outstanding Issues*, pp. 343-348.
- 1073 Hendy, C.H. and Wilson, A.T. (1968) Palaeoclimatic data from speleothems. *Nature* 219, 48-51.
- 1074 Hodge, E., McDonald, J., Fischer, M., Redwood, D., Hua, Q., Levchenko, V., Drysdale, R.,
1075 Waring, C. & Fink, D. (2011) Using the ^{14}C bomb pulse to date young speleothems.
1076 *Radiocarbon* 53, 345-357.
- 1077 Holland, H.D., Holland, H.J. and Munoz, J.L. (1964) The coprecipitation of cations with CaCO_3 -II.
1078 The coprecipitation of Sr^{2+} with calcite between 90° and 100°C . *Geochim. Cosmochim. Acta*
1079 28, 1287-1301.
- 1080 Howson, M.R., Pethybridge, A.D. and House, W.A. (1987) Synthesis and distribution coefficient of
1081 low-magnesium calcites. *Chem. Geol.* 64, 79-87.
- 1082 Huang, Y. and Fairchild, I.J. (2001) Partitioning of Sr^{2+} and Mg^{2+} into calcite under karst-analogue
1083 experimental conditions. *Geochim. Cosmochim. Acta* 65, 47-62.
- 1084 Huang, Y.M., Fairchild, I.J., Borsato, A., Frisia, S., Cassidy, N.J., McDermott, F. and
1085 Hawkesworth, C.J. (2001) Seasonal variations in Sr, Mg and P in modern speleothems (Grotta
1086 di Ernesto, Italy). *Chem. Geol.* 175, 429-448.
- 1087 Isola, I, Zanchetta, G, Drysdale, RN, Regattieri, E, Bini, M, Bajo, P, Hellstrom, JC, Baneschi, I,
1088 Lionello, P, Woodhead, J & Greig, A. (2019) The 4.2-ka event in the central Mediterranean:
1089 new data from a Corchia speleothem (Apuan Alps, central Italy). *Climate of the Past* 15, 135–
1090 151, doi:10.5194/cp-15-135-2019.
- 1091 Johnson, K.R., Hu, C., Belshaw, N.S. & Henderson, G.M. (2006) Seasonal trace-element and stable
1092 isotope variations in a Chinese speleothem: the potential for high-resolution paleomonsoon
1093 reconstruction. *Earth and Planetary Science Letters* 244, 394–407.
- 1094 Karmann, I., Cruz, F.W., Viana, O. and Burns, S.J. (2007) Climate influence on geochemistry
1095 parameters of waters from Santana-Pérolas cave system, Brazil. *Chem. Geol.* 244, 232-247.
- 1096 Katz, A. (1973) The interaction of magnesium with calcite during crystal growth at 25 - 90°C and
1097 one atmosphere. *Geochim. Cosmochim. Acta* 37, 1563-1586.
- 1098 Kelly, S.D., Newville, M.G., Cheng, L., Kemner, K.M., Sutton, S.R., Fenter, P., Sturchio, N.C. and
1099 Spötl, C. (2003) Uranyl incorporation in natural calcite. *Environ. Sci. Technol.* 37, 1284-
1100 1287.
- 1101 Kelly, S.D., Rasbury, E.T., Chattopadhyay, S., Kropf, A.J. and Kemner, K.M. (2006) Evidence of a
1102 stable uranyl site in ancient organic-rich calcite. *Environ. Sci. Technol.* 40, 2262-2268.

- 1103 Kitano, Y. and Oomori, T. (1971) The coprecipitation of uranium with calcium carbonate. *J. Ocean.*
1104 *Soc. Japan* 27, 34-42.
- 1105 Kligfield, R., Hunziker, J., Dallmeyer, R.D. and Schamel, S. (1986) Dating of deformation phases
1106 using K-Ar and $^{40}\text{Ar}/^{39}\text{Ar}$ techniques: results from the northern apennines. *J. Struct. Geol.* 8,
1107 781-798.
- 1108 Kolesar, P.T. and Riggs, A.C. (2004) Influence of depositional environment on Devils Hole calcite
1109 morphology and petrology, in: Sasowsky, I.D., Mylroie, J. (Eds.), *Studies of Cave Sediments.*
1110 Springer, Boston, MA, pp. 227-241.
- 1111 Lachniet, M.S. (2009) Climatic and environmental controls on speleothem oxygen-isotope values.
1112 *Quatern. Sci. Rev.* 28, 412-432.
- 1113 Langmuir, D. (1978) Uranium solution-mineral equilibria at low temperatures with applications to
1114 sedimentary ore deposits. *Geochim. Cosmochim. Acta* 42, 547-569.
- 1115 Lauritzen, S.E. and Lundberg, J. (1999) Speleothems and climate: a special issue of *The Holocene.*
1116 *The Holocene* 9, 643-647.
- 1117 Lea, D.W. and Spero, H.J. (1994) Assessing the reliability of paleochemical tracers: Barium uptake
1118 in the shells of planktonic foraminifera. *Paleocean.* 9, 445-452.
- 1119 Liu, Y.H., Henderson, G.M., Hu, C.Y., Mason, A.J., Charnley, N., Johnson, K.R. and Xie, S.C.
1120 (2013) Links between the East Asian monsoon and North Atlantic climate during the 8,200
1121 year event. *Nature Geoscience* 6, 117-120.
- 1122 Markowska, M., Baker, A., Andersen, M.S., Jex, C.N., Cuthbert, M.O., Rau, G.C., Graham, P.W.,
1123 Rutledge, H., Mariethoz, G., Marjo, C.E., Treble, P.C. and Edwards, N. (2016) Semi-arid zone
1124 caves: Evaporation and hydrological controls on $\delta^{18}\text{O}$ drip water composition and
1125 implications for speleothem paleoclimate reconstructions. *Quatern. Sci. Rev.* 131, 285-301.
- 1126 Matthey, D., Lowry, D., Duffet, J., Fisher, R., Hodge, E. and Frisia, S. (2008) A 53-year seasonally
1127 resolved oxygen and carbon isotope record from a modern Gibraltar speleothem:
1128 Reconstructed drip water and relationship to local precipitation. *Earth Planet. Sci. Lett.* 269,
1129 80-95.
- 1130 Matthey, D.P., Fairchild, I.J., Atkinson, T.C., Latin, J.-P., Ainsworth, M. and Durell, R. (2010)
1131 Seasonal microclimate control of calcite fabrics, stable isotopes and trace elements in modern
1132 speleothem from St Michaels Cave, Gibraltar. *Geol. Soc., London, Spec. Pub.* 336, 323-344.
- 1133 Mavromatis, V., Gautier, Q., Bosc, O. and Schott, J. (2013) Kinetics of Mg partition and Mg stable
1134 isotope fractionation during its incorporation in calcite. *Geochim. Cosmochim. Acta* 114, 188-
1135 203.
- 1136 McDermott, F. (2004) Paleo-climate reconstruction from stable isotope variations in speleothems: a
1137 review. *Quatern. Sci. Rev.* 23, 901-918.

- 1138 McDonald, J., Drysdale, R. and Hill, D. (2004) The 2002-2003 El Niño recorded in Australian cave
1139 drip waters: Implications for reconstructing rainfall histories using stalagmites. *Geophys. Res.*
1140 *Lett.* 31, doi:10.1029/2004GL020859.
- 1141 McDonald, J., Drysdale, R., Hill, D., Chisari, R. and Wong, H. (2007) The hydrochemical response
1142 of cave drip waters to sub-annual and inter-annual climate variability, Wombeyan Caves, SE
1143 Australia. *Chem. Geol.* 244, 605-633.
- 1144 Moseley, G.E., Edwards, R.L., Wendt, K.A., Cheng, H., Dublyansky, Y., Lu, Y., Boch, R. and
1145 Spötl, C. (2016) Reconciliation of the Devils Hole climate record with orbital forcing. *Science*
1146 351, 165-168.
- 1147 Mucci, A. and Morse, J.W. (1983) The incorporation of Mg^{2+} and Sr^{2+} into calcite overgrowths:
1148 influences of growth rate and solution composition. *Geochim. Cosmochim. Acta* 47, 217-233.
- 1149 Mucci, A. (1987) Influence of temperature on the composition of magnesian calcite overgrowths
1150 precipitated from seawater. *Geochim. Cosmochim. Acta* 51, 1977-1984.
- 1151 Neuser, R. D., Richter, D.K. (2007) Non-marine radiaxial fibrous calcites - examples of
1152 speleothems proved by electron backscatter diffraction. *Sed. Geol.* 194, 149-154.
- 1153 Nielsen, M.R., Sand, K.K., Rodriguez-Blanco, J.D., Bovet, N., Generosi, J., Dalby, K.N. and Stipp,
1154 S.L.S. (2016) Inhibition of Calcite Growth: Combined Effects of Mg^{2+} and SO_4^{2-} . *Crystal*
1155 *Growth & Design* 16, 6199-6207.
- 1156 Oomori, T., Kaneshima, H. and Maezato, Y. (1987) Distribution coefficient of Mg^{2+} ions between
1157 calcite and solution at 10-50°C. *Mar. Chem.* 20, 327-336.
- 1158 Orland, I.J., Burstyn, Y., Bar-Matthews, M., Kozdon, R., Ayalon, A., Matthews, A. and Valley,
1159 J.W. (2014) Seasonal climate signals (1990-2008) in a modern Soreq Cave stalagmite as
1160 revealed by high-resolution geochemical analysis. *Chemical Geology* 363, 322-333.
- 1161 Owen, R.A., Day, C.C, Hu, C.-Y., Liu, Y.-H., Pointing, M.D., Blättler, C.L. and Henderson, G.M.
1162 (2016) Calcium isotopes in caves as a proxy for aridity: modern calibration and application to
1163 the 8.2 kyr event. *Earth and Planetary Science Letters* 443, 129–138.
- 1164 Paquette, J. and Reeder, R.J. (1995) Relationship between surface structure, growth mechanism,
1165 and trace element incorporation in calcite. *Geochim. Cosmochim. Acta* 59, 735-749.
- 1166 Paton, C., Hellstrom, J., Paul, B., Woodhead, J. and Hergt, J. (2011) Iolite: Freeware for the
1167 visualisation and processing of mass spectrometric data. *J. Anal. At. Spectrom.* 26, 2508-
1168 2518.
- 1169 Piccini, L., Zanchetta, G., Drysdale, R.N., Hellstrom, J., Isola, I., Fallick, A.E., Leone, G., Doveri,
1170 M., Mussi, M., Mantelli, F., Molli, G., Lotti, L., Roncioni, A., Regattieri, E., Meccheri, M.
1171 and Vaselli, L. (2008) The environmental features of the Monte Corchia cave system (Apuan
1172 Alps, central Italy) and their effects on speleothem growth. *Int. J. Speleol.* 37 153-172.

- 1173 Pingitore, N.E. and Eastman, M.P. (1984) The experimental partitioning of Ba²⁺ into calcite. *Chem.*
1174 *Geol.* 45, 113-120.
- 1175 Pingitore, N.E. and Eastman, M.P. (1986) The coprecipitation of Sr²⁺ with calcite at 25°C and 1
1176 atm. *Geochim. Cosmochim. Acta* 50, 2195-2203.
- 1177 Plummer, N., Busenberg, E., Riggs, A.C. (2000) In-situ growth of calcite at Devils Hole, Nevada:
1178 comparison of field and laboratory rates to a 500,000 year record of near-equilibrium calcite
1179 growth. *Aqueous Geochemistry* 6, 257-274.
- 1180 Reed, M.H. (1982) Calculation of multicomponent chemical equilibria and reaction processes in
1181 systems involving minerals, gases and an aqueous phase. *Geochim. Cosmochim. Acta* 46,
1182 513-528.
- 1183 Reeder, R.J. and Grams, J.C. (1987) Sector zoning in calcite cement crystals: Implications for trace
1184 element distributions in carbonates. *Geochim. Cosmochim. Acta* 51, 187-194.
- 1185 Reeder, R.J., Nugent, M., Beck, K.M., Tait, C.D., Hess, W.P., Morris, D.E., Heald, S.M. and
1186 Lanzirotti, A. (2001) Coprecipitation of Uranium(VI) with Calcite: XAFS, micro-XAS, and
1187 luminescence characterization. *Geochim. Cosmochim. Acta* 65, 3491–3503.
- 1188 Reeder, R.J. and Paquette, J. (1990) Sector zoning in natural and synthetic calcites. *Sed. Geol.* 65,
1189 239-247.
- 1190 Reiners, P.W., Carlson, R.W., Renne, P.R., Cooper, K.M., Granger, D.E., McLean, N.M. and
1191 Schoene, B. (2017) *Geochronology and Thermochronology*. Wiley.
- 1192 Richards, D.A. and Dorale, J.A. (2003) Uranium-series chronology and environmental applications
1193 of speleothems. *Rev. Mineral. Geochem.* 52, 407-460.
- 1194 Rimstidt, J.D., Balog, A. and Webb, J. (1998) Distribution of trace elements between carbonate
1195 minerals and aqueous solutions. *Geochim. Cosmochim. Acta* 62, 1851-1863.
- 1196 Schwarcz, H.P., Harmon, R.S., Thompson, P. and Ford, D.C. (1976) Stable isotope studies of fluid
1197 inclusions in speleothems and their paleoclimatic significance. *Geochim. Cosmochim. Acta*
1198 40, 657-665.
- 1199 Spötl, C. and Matthey, D. (2012) Scientific drilling of speleothems - a technical note. *Int. J. Speleol.*
1200 41, 29-34.
- 1201 Tesoriero, A.J. and Pankow, J.F. (1996) Solid solution partitioning of Sr²⁺, Ba²⁺, and Cd²⁺ to
1202 calcite. *Geochim. Cosmochim. Acta* 60, 1053-1063.
- 1203 Treble, P., Chappell, J., Gagan, M., McKeegan, K. and Harrison, T. (2005) In situ measurement of
1204 seasonal δ¹⁸O variations and analysis of isotopic trends in a modern speleothem from
1205 southwest Australia. *Earth Planet. Sci. Lett.* 233, 17-32.

- 1206 Treble, P.C., Bradley, C., Wood, A., Baker, A., Jex, C.N., Fairchild, I.J., Gagan, M.K., Cowley, J.
1207 and Azcurra, C. (2013) An isotopic and modelling study of flow paths and storage in
1208 Quaternary calcarenite, SW Australia: implications for speleothem paleoclimate records.
1209 *Quatern. Sci. Rev.* 64, 90-103.
- 1210 Tremaine, D.M. and Froelich, P.N. (2013) Speleothem trace element signatures: A hydrologic
1211 geochemical study of modern cave dripwaters and farmed calcite. *Geochim. Cosmochim. Acta*
1212 121, 522-545.
- 1213 Ünal-Imer, E., Shulmeister, J., Zhao, J.X., Uysal, I.T. and Feng, Y.X. (2016) High-resolution trace
1214 element and stable/radiogenic isotope profiles of late Pleistocene to Holocene speleothems
1215 from Dim Cave, SW Turkey. *Palaeogeography, Palaeoclimatology, Palaeoecology* 452, 68-
1216 79.
- 1217 Wassenburg, J.A., Scholz, D., Jochum, K.P., Cheng, H., Oster, J., Immenhauser, A., Richter, D.K.,
1218 Häger, T., Hoffmann, D.L., Breitenbach, S.F.M., 2016. Determination of aragonite trace
1219 element partition coefficients from speleothem calcite-aragonite transitions. *Geochim.*
1220 *Cosmochim. Acta* 190, 347-367.
- 1221 Weber, M., Scholz, D., Schröder-Ritzrau, A., Deininger, M., Spötl, C., Lugli, F., Mertz-Kraus, R.,
1222 Jochum, K.P., Fohlmeister, J., Stumpf, C.F. and Riechelmann, D.F.C. (2018) Evidence of
1223 warm and humid interstadials in central Europe during early MIS 3 revealed by a multi-proxy
1224 speleothem record. *Quaternary Science Reviews* 200, 276-286.
- 1225 Weremeichik, J.M., Gabitov, R.I., Thien, B.M.J. and Sadekov, A. (2017) The effect of growth rate
1226 on uranium partitioning between individual calcite crystals and fluid. *Chem. Geol.* 450, 145-
1227 153.
- 1228 Winograd, I.J., Coplen, T.B., Landwehr, J.M., Riggs, A.C., Ludwig, K.R., Szabo, B.J., Kolesar,
1229 P.T. and Revesz, K.M. (1992) Continuous 500,000-year climate record from vein calcite in
1230 Devils Hole, Nevada. *Science* 258, 255-260.
- 1231 Wong, C.I., Banner, J.L. and Musgrove, M. (2015) Holocene climate variability in Texas, USA: An
1232 integration of existing paleoclimate data and modeling with a new, high-resolution
1233 speleothem record. *Quaternary Science Reviews* 127, 155-173.
- 1234 Woodhead, J., Hellstrom, J., Maas, R., Drysdale, R., Zanchetta, G., Devine, P. and Taylor, E.
1235 (2006) U-Pb geochronology of speleothems by MC-ICPMS. *Quat. Geochronol.* 1, 208-221.
- 1236 Woodhead, J.D., Hellstrom, J., Hergt, J.M., Greig, A. and Maas, R. (2007) Isotopic and Elemental
1237 Imaging of Geological Materials by Laser Ablation Inductively Coupled Plasma-Mass
1238 Spectrometry. *Geostand. Geoanal. Res.* 31, 331-343.
- 1239 Yoshimura, T., Suzuki, A. and Iwasaki, N. (2015) Ba, B, and U element partitioning in magnesian
1240 calcite skeletons of *Octocorallia* corals. *Biogeosci. Discuss.* 12, 413-444.

- 1241 Zanchetta, G., Drysdale, R.N., Hellstrom, J.C., Fallick, A.E., Isola, I., Gagan, M.K. and Pareschi,
1242 M.T. (2007) Enhanced rainfall in the Western Mediterranean during deposition of sapropel
1243 S1: stalagmite evidence from Corchia cave (Central Italy). *Quatern. Sci. Rev.* 26, 279-286.
- 1244 Zhou, H., Chi, B., Lawrence, M., Zhao, J., Yan, J., Greig, A. and Feng, Y. (2008) High-resolution
1245 and precisely dated record of weathering and hydrological dynamics recorded by manganese
1246 and rare-earth elements in a stalagmite from Central China. *Quat. Res.* 69, 438-446.
1247

Table 1: Instrumental operating conditions for the LA-ICP-MS.

<i>Agilent 7700x ICP-MS</i>	
Forward power	1300 W
Reflected power	2 W
Sample depth	3 mm
Dwell time	0.01 s
Carrier gas	0.89 L min ⁻¹
Masses measured (m/z)	²⁵ Mg, ⁴³ Ca, ⁸⁸ Sr, ¹³⁸ Ba, ²³⁸ U
 <i>Helex laser-ablation system</i>	
Lambda Physik Compex 110 ArF excimer	193 nm
Laser fluence	~5 J cm ⁻²
Data collection spot size	7 μm
Data collection repetition rate	5 Hz
Helium gas to cell	500 mL min ⁻¹
Ablation time	15 s
Final data acquisition window	~5 s

Table 2: Laghetto Basso pool water chemistry measured on samples taken between 25 May 2009 and 23 March 2012. A summary of data measured between 1997 and 2006 (from Piccini et al. 2008) are shown in the bottom section of the table. Further water chemistry variables are shown in Supplementary Table 2.

<i>Date</i>	<i>Temp.</i> (°C)	<i>pH</i>	<i>HCO₃⁻</i> (mg L ⁻¹)	<i>Ca²⁺</i> (mg L ⁻¹)	<i>Mg²⁺</i> (mg L ⁻¹)	<i>Sr²⁺</i> (µg L ⁻¹)	<i>Ba²⁺</i> (µg L ⁻¹)	<i>U</i> (µg L ⁻¹)	<i>Mg/Ca</i> (mol/mol)	<i>Sr/Ca</i> (mmol/mol)	<i>Ba/Ca</i> (mmol/mol)	<i>U/Ca</i> (mmol/mol)
22/05/09	8.0	8.3	151.3	29.5	20.9	53	25	5.2	1.168	0.822	0.247	0.030
17/06/09	7.3	8.4	157.4	30.2	21.0	55	28	5.1	1.146	0.833	0.271	0.028
28/07/09	8.1	8.0	153.7	30.1	21.0	68	29	8.0	1.150	1.033	0.281	0.045
28/08/09	8.0	8.4	154.4	29.7	20.7	65	28	7.9	1.149	1.001	0.275	0.045
02/10/09	8.1	8.3	152.5	29.8	19.6	53	23	7.5	1.084	0.814	0.225	0.042
14/11/09	7.9	8.2	143.4	28.0	17.5	54	23	7.9	1.030	0.882	0.240	0.048
14/12/09	8.0	8.3	151.3	29.0	20.4	54	23	7.7	1.160	0.852	0.231	0.045
24/02/10	8.0	8.2	164.7	29.9	21.8	57	24	6.4	1.202	0.872	0.234	0.036
27/03/10	8.0	8.1	152.5	29.4	21.2	53	22	5.6	1.189	0.825	0.218	0.032
19/04/10	7.9	8.4	154.4	28.5	21.0	53	23	5.5	1.215	0.851	0.236	0.032
31/05/10	7.8	8.3	158.6	28.6	20.5	56	26	7.2	1.182	0.896	0.265	0.042
29/06/10	7.8	8.3	149.5	30.0	20.8	58	25	6.9	1.143	0.884	0.243	0.039
05/08/10	7.9	8.3	148.3	28.6	21.0	58	27	7.2	1.211	0.928	0.276	0.042
01/09/10	7.9	8.3	148.3	28.9	20.8	56	24	7.0	1.187	0.886	0.242	0.041
30/09/10	7.9	8.3	143.4	29.0	20.9	53	23	6.6	1.188	0.836	0.231	0.038
29/10/10	7.9	8.2	146.4	27.1	20.8	58	24	7.1	1.265	0.979	0.258	0.044
25/11/10	7.9	8.1	156.8	29.9	20.3	56	23	7.2	1.119	0.857	0.225	0.041
29/12/10	7.9	8.1	149.5	29.3	21.0	56	22	7.1	1.182	0.874	0.219	0.041
03/02/11	7.5	8.2	147.6	28.4	20.7	56	24	6.9	1.202	0.902	0.247	0.041
10/03/11	8.0	8.2	154.4	29.4	19.8	55	22	6.6	1.110	0.856	0.218	0.038
05/04/11	7.8	8.2	152.5	28.1	21.1	54	21	6.5	1.238	0.879	0.218	0.039
11/05/11	7.7	8.2	148.3	28.5	21.4	56	22	6.5	1.238	0.899	0.225	0.038
24/06/11	7.6	8.2	158.6	28.8	21.7	55	23	6.4	1.242	0.874	0.233	0.037
11/07/11	7.8	8.1	148.9	29.1	21.4	55	23	6.3	1.212	0.865	0.231	0.036
09/08/11	7.4	8.1	146.4	27.8	20.4	57	23	6.4	1.210	0.938	0.241	0.039
06/10/11	7.9	8.2	151.3	29.7	21.8	56	22	6.3	1.210	0.862	0.216	0.036
07/11/11	8.4	8.1	144.0	28.6	20.7	55	22	6.1	1.193	0.880	0.225	0.036
23/03/12	8.1	7.9	151.3	32.0	20.7	52	21	5.7	1.067	0.743	0.192	0.030
Mean	7.9	8.2	151.4	29.1	20.7	56.0	23.8	6.7	1.175	0.879	0.238	0.039
2σ	0.4	0.2	10.0	1.8	1.6	6.9	4.2	1.6	0.116	0.116	0.042	0.010
% CV (2σ)			3.3	3.3	3.9	6.1	8.9	11.9	9.3	13.2	17.6	25.6
n	28	28	28	28	28	28	28	28	28	28	28	28
<i>Summary of 1997 – 2006 data (Piccini et al. 2008)</i>												
Mean		8.2	154.0	30.3	20.6				1.121			
2σ		0.2	10.0	2.0	1.8				0.123			
n		10	10	10	10				10			

Table 3: Results of ICP-MS solution analyses conducted on calcite abraded from the actively growing surface of core CD3-12. Analyses were conducted at two laboratories, the University of Melbourne (UoM) and the Australian Nuclear Science and Technology Organisation (ANSTO). The reduced χ -squared statistics on the paired means for all four ratios are less than the critical value of χ at $p = 0.05$. Therefore, each pair can be regarded as being drawn from the same population, and the data combined by calculating the error-weighted mean (EW mean); the corresponding 2σ is the error-weighted 95% uncertainty. CV % is the per cent coefficient of variation calculated using 2σ .

Sample	Mg/Ca (mol/mol)		Sr/Ca (mmol/mol)		Ba/Ca (mmol/mol)		U/Ca (μ mol/mol)	
	UM	ANSTO	UM	ANSTO	UM	ANSTO	UM	ANSTO
CD3-12-A	0.0494	0.0487	0.0873	0.0895	0.0209	0.0204	0.4793	0.4934
CD3-12-B	0.0497	0.0485	0.0878	0.0881	0.0220	0.0201	0.5196	0.5026
CD3-12-C	0.0500	0.0497	0.0887	0.0909	0.0214	0.0207	0.5020	0.5051
CD3-12-D	0.0496	0.0491	0.0859	0.0874	0.0213	0.0201	0.5170	0.5041
CD3-12-E	0.0500	0.0494	0.0871	0.0887	0.0215	0.0199	0.5078	0.4941
CD3-12-F	0.0495	0.0485	0.0848	0.0879	0.0206	0.0195	0.5447	0.5578
CD3-12-G	0.0496	0.0476	0.0868	0.0878	0.0220	0.0199	0.5272	0.5193
CD3-12-H	0.0494	0.0488	0.0857	0.0867	0.0214	0.0195	0.5175	0.5107
CD3-12-I	0.0494	0.0487	0.0862	0.0898	0.0217	0.0205	0.5420	0.5173
CD3-12-J	0.0498	0.0495	0.0869	0.0880	0.0218	0.0198	0.5229	0.5137
CD3-12-K	0.0503	0.0504	0.0886	0.0896	0.0230	0.0204	0.5453	0.5093
CD3-12-L	0.0499	0.0490	0.0871	0.0893	0.0221	0.0200	0.5320	0.5108
CD3-12-M	0.0498	0.0488	0.0844	0.0878	0.0205	0.0197	0.4997	0.4730
CD3-12-N	0.0503	0.0508	0.0875	0.0921	0.0218	0.0206	0.5172	0.5114
CD3-12-O	0.0495	0.0488	0.0876	0.0876	0.0228	0.0197	0.5201	0.4878
Mean	0.0497	0.0491	0.0868	0.0888	0.0216	0.0201	0.5196	0.5074
$\pm 2\sigma$	0.0006	0.0016	0.0025	0.0029	0.0014	0.0008	0.0359	0.0372
% CV (2σ)	1.2	3.2	2.9	3.3	1.9	3.9	6.9	7.3
r^2	0.81*		0.54*		0.16		0.67*	
% difference	1.3		-2.2		7.3		2.4	
EW mean $\pm 2\sigma$	0.0496	0.0006	0.0877	0.0029	0.0205	0.0007	0.5137	0.0258
% CV (2σ)	1.2		3.3		3.4		5.0	

Table 4: (a) Summary of Mg, Sr, Ba and U concentrations from the seven traverses of the outer rim of CD3-12 measured by LA-ICP-MS. The mean and 2 s.d. of each traverse for each element is shown, as is the overall mean (bold) and 2 s.d. The % CV is the per cent coefficient of variation calculated using 2 s.d.

<i>Traverse number</i>	<i>Number of spots</i>	<i>Mg (ppm)</i>	$\pm 2\sigma$	<i>Sr (ppm)</i>	$\pm 2\sigma$	<i>Ba (ppm)</i>	$\pm 2\sigma$	<i>U (ppm)</i>	$\pm 2\sigma$
1	11	10992	1017	70.8	8.0	24.4	3.2	1.27	0.19
2	21	11382	791	72.4	6.3	24.2	3.4	1.02	0.26
3	16	11380	503	72.1	3.3	24.6	2.1	1.38	0.14
4	17	11382	693	72.8	4.3	25.7	2.0	1.40	0.09
5	17	11396	794	72.6	6.2	26.5	7.1	1.43	0.15
6	28	11607	1094	75.2	9.9	25.6	6.5	0.84	0.36
7	10	11097	597	68.3	5.6	23.5	2.4	1.32	0.15
Mean $\pm 2\sigma$		11377	896	72.6	7.7	25.1	4.9	1.19	0.65
% CV (2σ)		7.9		10.6		19.6		55.1	

Table 5: Calcite partition coefficients for Mg, Sr, Ba and U from this study. Coefficients are also shown from previous studies cave and cave-analogue (lab) studies for comparison. For Laghetto Basso, D_x results for both surface calcite [X/Ca]/pool water [X/Ca] (Table 3) and LA-ICP-MS outer rim [X/Ca]/pool water [X/Ca] (Table 5) are shown.

Source of data	Setting	Temp. (°C)	D_{Mg}		D_{Sr}		D_{Ba}		D_U	
			Max-Min	Mean 1σ	Max-Min	Mean 1σ	Max-Min	Mean 1σ	Max-Min	Mean 1σ
This study	Solution ICP-MS	Cave	8	0.042 ±0.002	-	0.100 ±0.007	-	0.086 ±0.008	-	0.013 ±0.002
	LA-ICP-MS			0.042 ±0.003	-	0.094 ±0.008	-	0.076 ±0.018	-	0.013 ±0.005
Tremaine & Froehlich (2013)	Cave	19	0.047-0.014	0.027 ±0.008	0.120-0.037	0.090 ±0.022				
Fairchild et al. (2010)	Cave	6	0.020-0.015	0.018 ±0.003	0.130-0.079	0.110 ±0.027	-	-	-	-
Karman et al. (2007)	Cave	19	-	0.023 -	-	0.059 -	-	-	-	-
Huang et al. (2001)	Cave	7	0.016-0.012	0.014 ±0.003	0.16-0.15	0.155 ±0.007	-	-	-	-
Gascoyne (1983)	Cave	7	0.021-0.013	0.017 ±0.003	0.232-0.127	0.175 ±0.038	-	-	-	-
		23	0.057-0.040	0.045 ±0.006	0.298-0.088	0.206 ±0.092	-	-	-	-
Holland et al. (1964a)	Cave	16	-	-	0.280-0.130	0.190 ±0.016	-	-	-	-
Day & Henderson (2013)	Lab	7	-	0.012 ±0.001	-	0.130 ±0.007	-	-	-	0.110 ±0.011
		15	-	0.013 ±0.001	-	0.120 ±0.007	-	-	-	0.120 ±0.011
		25	-	0.016 ±0.001	-	0.130 ±0.006	-	0.110 ±0.008	-	0.033 ±0.011
		35	-	0.020 ±0.001	-	0.120 ±0.006	-	0.110 ±0.009	-	0.062 ±0.012
Huang & Fairchild (2001)	Lab	15	0.022-0.016	0.020 ±0.003	0.079-0.068	0.072 ±0.006	-	-	-	-
		25	0.033-0.030	0.031 ±0.001	0.077-0.071	0.076 ±0.003	-	-	-	-